NAVAL POSTGRADUATE SCHOOL
MONTEREY, CALIFORNIA

THESIS

THE EFFECT OF STIFFENER SMEARING IN A
SHIP-LIKE BOX STRUCTURE SUBJECTED TO AN
UNDERWATER EXPLOSION

by

Keith A. Beiter

June 1998

Thesis Advisor: Young S. Shin

Approved for public release; distribution is unlimited.

REPORT DOCUMENTATION PAGE

Form Approved OMB No. 0704-0188

1. AGENCY USE ONLY *(Leave blank)*	2. REPORT DATE June 1998.	3. REPORT TYPE AND DATES COVERED Master's Thesis	
4. TITLE AND SUBTITLE: THE EFFECT OF STIFFENER SMEARING IN A SHIP-LIKE BOX STRUCTURE SUBJECTED TO AN UNDERWATER EXPLOSION		**5. FUNDING NUMBERS**	
6. AUTHOR(S) Beiter, Keith A.			
7. PERFORMING ORGANIZATION NAME(S) AND ADDRESS(ES) Naval Postgraduate School Monterey CA 93943-5000		**8. PERFORMING ORGANIZATION REPORT NUMBER**	
9. SPONSORING/MONITORING AGENCY NAME(S) AND ADDRESS(ES)		**10. SPONSORING/MONITORING AGENCY REPORT NUMBER**	

11. SUPPLEMENTARY NOTES
The views expressed here are those of the authors and do not reflect the official policy or position of the Department of Defense or the U.S. Government.

12a. DISTRIBUTION/AVAILABILITY STATEMENT Approved for public release; distribution is unlimited.	12b. DISTRIBUTION CODE

13. ABSTRACT *(maximum 200 words)*

Shock trials for naval vessels are a requirement for each new class of surface ships in the U.S. Navy. With understanding the technology of underwater shock analysis and considering the rising costs of conducting actual shock tests, computer simulation of shock trials is becoming more and more attractive. Unfortunately, finite element models can be quite large and require sufficient amounts of computer memory and time to run a shock analysis. This thesis investigates the effects of reducing the element size of a ship-like box model subjected to an underwater explosion. Known as smearing, this process combines the density and stiffness properties of the removed elements into the remaining material of the model. Positive results from computer simulation could greatly affect the manner in which shock trials are conducted with future ship classes.

14. SUBJECT TERMS Underwater Explosion, Smearing, Surface Model			**15. NUMBER OF PAGES** 70
			16. PRICE CODE
17. SECURITY CLASSIFICATION OF REPORT Unclassified	**18. SECURITY CLASSIFICATION OF THIS PAGE** Unclassified	**19. SECURITY CLASSIFICATION OF ABSTRACT** Unclassified	**20. LIMITATION OF ABSTRACT** UL

THE EFFECT OF STIFFENER SMEARING IN A SHIP-LIKE BOX STRUCTURE SUBJECTED TO AN UNDERWATER EXPLOSION

Keith A. Beiter
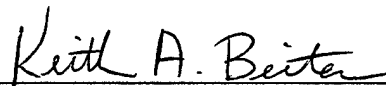Lieutenant, United States Navy
B.S., United States Naval Academy, 1992

Submitted in partial fulfillment of the
requirements for the degree of

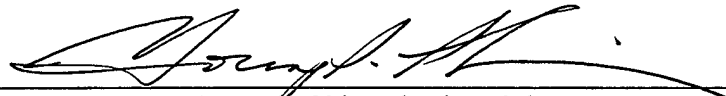## MASTER OF SCIENCE IN MECHANICAL ENGINEERING

from the

NAVAL POSTGRADUATE SCHOOL
June 1998

Author: _____
Keith A. Beiter

Approved by: _____
Young S. Shin, Thesis Advisor

_____
Terry R. McNelley, Chairman
Department of Mechanical Engineering

iii

ABSTRACT

Shock trials for naval vessels are a requirement for each new class of surface ships in the U.S. Navy. With understanding the technology of underwater shock analysis and considering the rising costs of conducting actual shock tests, computer simulation of shock trials is becoming more and more attractive. Unfortunately, finite element models can be quite large and require sufficient amounts of computer memory and time to run a shock analysis. This thesis investigates the effects of reducing the element size of a ship-like box model subject to an underwater explosion. Known as smearing, this process combines the density and stiffness properties of the removed elements into the remaining material of the model. Positive results from computer simulation could greatly affect the manner in which shock trials are conducted with future ship classes.

TABLE OF CONTENTS

ACKNOWLEDGEMENTS

I. INTRODUCTION

A.   BACKGROUND

During the Second World War, the United States Navy began to investigate more thoroughly the damage sustained by surface ships due to impacting shock waves, or pressure pulses, produced from underwater explosions such as those of non-contact mines. These pressure pulses, applied to a large area of the ship's hull, can have a serious negative effect on the ship structure as well as the equipment located onboard. The purpose of these tests was to improve the survivability of, while minimizing damage to, the ship's hull and onboard equipment and systems. Since then, the Navy has developed guidelines and specifications for shock testing new classes of ships and the equipment located in them. Known as shock trials, these tests are required for all surface ship classes that must be capable of operating in a combat environment. Shock hardening criteria apply to onboard systems and equipment that perform or directly support mission-essential functions on these ships. The goal of shock hardness testing is the development and installation of system improvements to prevent or minimize the broad degrading effects of shock on mission performance [Ref. 1]. Further guidelines on shock hardening of surface ships are outlined in OPNAVINST 9072.2 (reference 1).

Unfortunately, conducting ship shock trials can be time consuming and expensive. Initial planning stages for the shock trial of the USS John Paul Jones (DDG 53) began four years prior to the actual test date while the ship was still undergoing construction at Bath Iron Works, Maine. The entire endeavor involved over 50 government agencies. Originally scheduled for February 1994 when weather conditions are most favorable, the shock trial was delayed 3 months due to a lawsuit filed against the Navy by environmentalist groups concerned over the well being of sea life in the testing area. When testing occurred in June 1994, only two of the four required tests could be carried out because of inclement weather. The remaining two shock tests could not be performed. Further modifications to the ship's schedule to accommodate the two tests were not feasible since the three-month delay had already affected the ship's post trial delivery date and deployment preparations [Ref. 2].

1

With the advent and ongoing advances in computer technology, finite element modeling has become more and more refined. In view of the time and cost involved in planning and conducting an actual shock trial, simulating these tests on a finite element computer model would be desirable in many aspects. Finite element modeling codes such as True*Grid*®, MSC/PATRAN, and I-DEAS have enabled generation of detailed finite element models in a timely manner. In analyzing finite element models, higher detailed model meshes provide more reliable results than do less refined meshes. Highly detailed models, of course, do require valuable computer memory and time when performing structural analysis. Reducing the complexity of a finite element model mesh is one method in which to solve the problem of time consuming and expensive computer usage. Even though a less refined mesh may affect the results of the analysis as mentioned above, acceptable results can still be obtained depending on how much the model complexity is reduced.

B.   SCOPE OF RESEARCH

This paper investigates the effects of reducing the complexity, or element size, of a finite element model subject to an underwater explosion. The reducing process is known as smearing and combines the density and stiffness properties of the removed elements into the remaining material of the model. The model to be considered in this study is a ship-like box model with two bulkheads, a keel, and beam stiffeners. Analysis of the model response is conducted using the Underwater Shock Analysis (USA)/LS-DYNA. The purpose of this thesis is to compare responses of smeared models to those of the original in order to ascertain the reliability of this model reduction method. With reliable results, computer simulation of ship shock trials could be a dependable, cost effective, and time efficient manner for validating surface ship shock hardening requirements.

II. UNDERWATER EXPLOSIONS

A.   UNDERWATER SHOCK PHENOMENA

The sequence of events for an underwater explosion is fairly complex. When a high explosive (TNT, RDX, HBX-1, etc.) is detonated, the original solid material of the explosive is converted into a high temperature and pressure gas within nanoseconds. The pressure wave that is formed originates in one section of the explosive and propagates throughout the remainder of the explosive. As this pressure wave propagates, it initiates the chemical reaction that creates more pressure waves. The pressure wave velocity steadily increases within the solid explosive until it exceeds the speed of sound in the explosive. Therefore, a shock wave is produced. The shock wave propagates through the solid at a constant speed and then, with the high temperature and pressure behind the shock front, into the surrounding medium [Ref. 3].

The high-pressure gas that results from the explosion rapidly expands outward in a radial manner, Fig. 1, and imparts an outward velocity on the surrounding water as
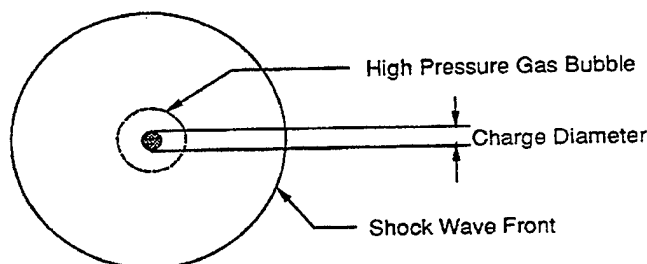
Figure 1. Gas Bubble and Shock Wave from an Underwater Explosion

well. Initially, the pressure is much greater than the atmospheric and hydrostatic pressure that opposes it and is therefore compressive in nature. At detonation, the pressure rise is discontinuous and decays exponentially with time as shown in Fig. 2. Duration of the pressure disturbance lasts only for a few milliseconds. The shock wave is characterized

3
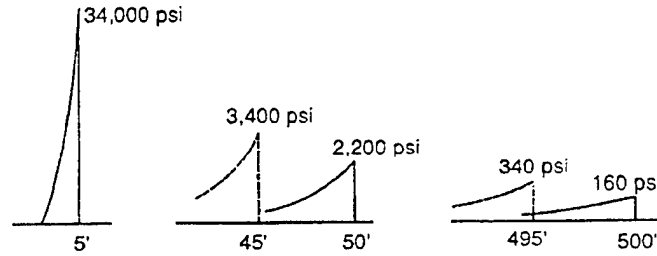
Figure 2. Shock Wave Profiles From a 300 lb. TNT Charge [Ref. 3]

by a propagation velocity that is several times that of acoustic velocity, 5,000 ft/sec, near the charge which then falls rapidly to acoustic velocity as it travels outward in the water. Additionally, the pressure profile of the shock wave is proportional to the inverse of the distance from the charge, 1/d, and the wave profile gradually broadens as it spreads out [Ref. 3]. Empirical equations have been determined to define the profile of the shock wave:

$$P(t) = P_{max} e^{-\frac{t-t_1}{\theta}} \quad \text{(psi)}$$

$$P_{max} = K(\frac{W^{\frac{1}{3}}}{R})^A \quad \text{(psi)}$$

$$\theta = KW^{\frac{1}{3}}(\frac{W^{\frac{1}{3}}}{R})^A \quad \text{(msec)}$$

where P is the magnitude of the pressure wave at time t, P_{max} is the peak magnitude of the pressure in the shock front, $t-t_1$ is the elapsed time after the arrival of the shock, θ is the decay constant which describes the exponential decay of the pressure wave at one-third of its maximum value, R is the distance from the explosive to the target in feet, and A is a constant that depends on the charge type.

Depending on the charge location relative to the surface and the bottom, other effects are characteristic of an underwater shock. Surface cut-off is a tension wave, as

4

opposed to a compressive wave, that is produced from the rarefaction of the shock wave off of the surface. Bottom reflection is the bouncing of the shock wave off of the bottom of the body of water; a compressive wave. Refraction causes the shock wave to travel through the bottom of the body of water before emerging again; also a compressive wave. Surface effects also occur as a result of an underwater explosion. A spray dome appears first which is caused by the shock wave. Water plumes follow the spray dome and are a result of the bubble pressure pulses. A bubble pressure pulse is produced when the gas bubble collapses during its oscillation and migration to the surface [Ref. 4].

B.   FLUID-STRUCTURE INTERACTION

When an object such as a ship or submarine is in the vicinity of an underwater explosion, the shock pressure pulses produced by the explosion impinge upon the surface of the structure. A fluid-structure interaction takes place as the pressure pulse acts upon the flexible surface of the structure. The entire structure is excited by the pressure pulse and responds in a dynamic manner. Taylor flat plate theory is the simplest case of fluid-structure interaction, first introduced by G. I. Taylor. In this case, an infinite, air-backed plate is acted upon by an incident plane shock wave as shown below in Fig. 3.
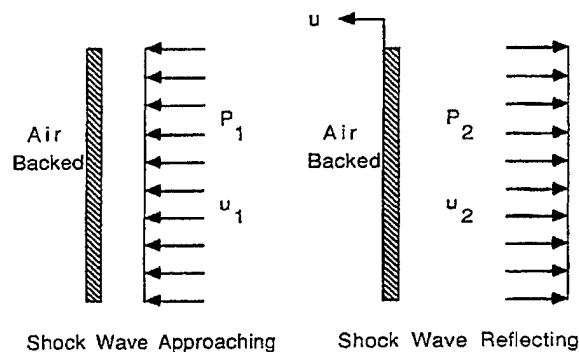
Figure 3. Taylor Flat Plate Theory: Incident and Reflected Pressure Waves

Once the shock wave strikes the plate, a reflected shock wave leaves the plate. According to Newton's second law of motion as shown in Eq. (2.1),

$$m\frac{du}{dt} = P_1 + P_2 \tag{2.1}$$

where m is the mass of the plate per unit area, u is the velocity of the plate after being subjected to the shock wave, $P_1(t)$ is the incident wave pressure and $P_2(t)$ is the reflected, or scattered, wave pressure. Define the fluid particle velocities behind the incident and reflected shock waves as $u_1(t)$ and $u_2(t)$. The velocity of the plate is then defined by Eq. (2.2),

$$u(t) = u_1(t) - u_2(t) \tag{2.2}$$

For the one dimensional plane wave, the wave equation is $P = \rho Cu$. It follows that the incident and reflected shock wave pressures, Eqs. (2.3) and (2.4), are

$$P_1 = \rho Cu_1 \tag{2.3}$$

$$P_2 = \rho Cu_2 \tag{2.4}$$

where ρ is the fluid density and C is the acoustic velocity in water. Substituting the above pressure Eqs (2.3) and (2.4) into the velocity Eq. (2.2) results in the incident shock pressure being defined as Eq. (2.5)

$$P_1(t) = P_{max}e^{-\frac{t}{\theta}} \tag{2.5}$$

Solving for the reflected shock pressure yields Eq. (2.6),

$$P_2(t) = P_1 - \rho Cu = P_{max}e^{-\frac{t}{\theta}} - \rho Cu \tag{2.6}$$

where t is the time after the shock wave arrives at the target. Now the equation of motion, Eq. (2.1) can be rewritten as Eq. (2.7),

$$m(\frac{du}{dt}) + \rho Cu = 2P_{max}e^{-\frac{t}{\theta}} \tag{2.7}$$

which is a first order, linear differential equation. The solution, u(t), of the differential equation is expressed in Eq. (2.8) as

$$u = \frac{2P_{max}\theta}{m(1-\beta)}[e^{-\frac{\beta t}{\theta}} - e^{-\frac{t}{\theta}}] \tag{2.8}$$

with $\beta = \rho C\theta/m$ and $t>0$. The total pressure that impinges on the plate is defined as Eq. (2.9),

$$P_1 + P_2 = P_{max}[\frac{2}{1-\beta}e^{-\frac{t}{\theta}} - \frac{2\beta}{1-\beta}e^{-\frac{\beta t}{\theta}}] \tag{2.9}$$

As the value of β becomes larger, as in the case of a lightweight plate, the total pressure will become negative at a very early time. However, since water cannot support tension, negative pressure cannot exist. Therefore, as the water pressure reduces to vapor pressure at the surface of the plate, cavitation occurs. At this point, the pressure in front of the plate has been cut off and the plate has reached its maximum velocity [Ref. 4].

The total pressure relationship shown above in Eq. (2.9) is a critical component in solving the fluid-structure interaction problem. In 1971, Thomas L. Gears described a matrix of differential equations in time for the approximate treatment of acoustic fluid-structure interaction. It is called the Doubly Asymptotic Approximation (DAA) and is accurate at both low and high frequencies and at early and late times. The DAA represents the surrounding fluid of the structure through the interaction of state variables pertaining only to the structure's wet surface [Ref. 5]. The fluid equation, Eq. (2.10), of the DAA is

$$[M_f]\{\dot{p}_2\} + \rho c[A_f]\{p_2\} = \rho c[M_f]\{\dot{u}_2\} \tag{2.10}$$

where $[M_f]$ is the symmetric fluid mass matrix for the wet-surface fluid mesh, $\{p_2\}$ and $\{\dot{p}_2\}$ are the nodal pressure vector and its first time derivative of the scattered wave, c is the acoustic velocity of water, $[A_f]$ is the diagonal area matrix associated with the fluid elements, and $\{\dot{u}_2\}$ is the scattered wave velocity vector. An object in the fluid will have a structural response defined as follows in Eq. (2.11),

$$[M_s]\{\ddot{x}\} + [C_s]\{\dot{x}\} + [K_s]\{x\} = \{f\} \tag{2.11}$$

7

where $[M_s]$ is the mass matrix, $[C_s]$ is the dampening matrix, $[K_s]$ is the matrix, stiffness $\{\ddot{x}\}$ is the acceleration vector, $\{\dot{x}\}$ is the velocity vector, and $\{x\}$ is the displacement vector of the structure and $\{f\}$ is the external force vector. Compatibility at the wet surface is described by Eqs. (2.12) and (2.13)

$$\{f\} = -[G][A_f](\{p_1\} + \{p_2\}) \tag{2.12}$$

and

$$[G]^T\{\dot{x}\} = \{u_1\} + \{u_2\} \tag{2.13}$$

where $[G]$ is the transformation matrix that relates the surface nodal forces of the fluid and structure. The "T" superscript indicates the transpose of the matrix. Substituting Eq. (2.12) into (2.11) and solving for $\{u_2\}$ in Eq. (2.13), taking the first time derivative, and substituting into Eq. (2.10) results in Eqs. (2.14) and (2.15),

$$[M_s]\{\ddot{x}\} + [C_s]\{\dot{x}\} + [K_s]\{x\} = -[G][A_f](\{p_1\} + \{p_2\}) \tag{2.14}$$

and

$$[M_f]\{\dot{p}_2\} + \rho c[A_f]\{p_2\} = \rho c M_f([G]^T\{\ddot{x}\} - \{\dot{u}_1\}) \tag{2.15}$$

The USA code solves Eqs. (2.14) and (2.15) simultaneously by using a staggered solution procedure that is unconditionally stable with respect to the time step used [Ref. 6]. Once this system of equations is solved, desired response results such as displacement, velocity, and acceleration can be studied.

III. MODEL CONSTRUCTION, TESTING AND SMEARING

A.   MODEL CONSTRUCTION AND TESTING PROCEDURE

Model construction and testing involves pre-processing, conversion, analysis, and post-processing programs. A flow chart of the model building and testing procedure is shown below in Fig. 4.
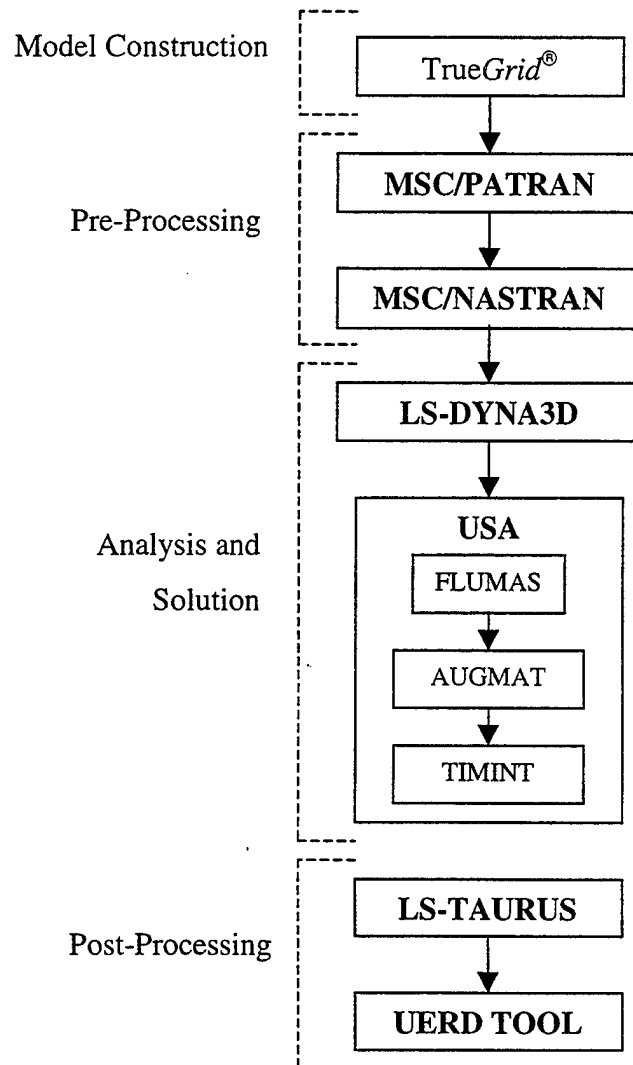
Model Construction

Pre-Processing

Analysis and
Solution

Post-Processing

TrueGrid®

MSC/PATRAN

MSC/NASTRAN

LS-DYNA3D

USA

FLUMAS

AUGMAT

TIMINT

LS-TAURUS

UERD TOOL

Figure 4. Flow Chart. Model Construction and Testing

The box-like ship model for this study was created using a finite element mesh generator known as True*Grid*®. This computer program produces hexahedral and quadrilateral (quad) elements from geometric model data that is input by the user [Ref. 7]. After necessary material properties are defined, True*Grid*® writes the model to an output file in NASTRAN format. The NASTRAN input file, or deck, is then entered into PATRAN, a finite element mesh generator, analyzer, and pre- and post-processor [Ref. 8]. In PATRAN, the NASTRAN deck is then set up for normal modal analysis in order to verify a correct dynamic response of the box structure to ensure that the model is constructed properly. Modal analysis is performed by NASTRAN, a finite element analysis code that allows for a number of different analysis types [Ref. 8]. The next step is to convert the NASTRAN deck into a LS-DYNA input deck. LS-DYNA is a finite element code that provides the means for analyzing structures under a variety of load conditions [Ref. 9]. For this particular study, LS-DYNA3D was coupled with the USA code to obtain the results to the underwater shock phenomenon. The USA code solves for the transient response of a partially or totally submerged structure subjected to an acoustic shock wave [Ref. 6]. Once the transient analysis is complete, the response of the structure is converted into ASCII files using LS-TAURUS. This program is used for post-processing two and three dimensional finite element analysis codes [Ref. 9]. Responses from the structure were then graphed using the Underwater Explosion Research Division (UERD) Tool, a PC based program for displaying a variety of shock responses.

The box structure analyzed in this research, shown in Fig. 5, contained two bulkheads and a keel. It was 120-in long, 24-in wide, and 24-in deep. The bottom, sides, and bulkheads of the box were made of 1/4-in steel plating with a weight density of 0.284 lbf/in^3 and an elastic modulus (Young's modulus, E) of 30 x 10^6 psi. Steel stiffeners with the same mass density and elastic modulus as the plate material were added to the bottom, sides, and bulkheads to increase the model rigidity. Their cross section dimensions were 0.125-in thick by 2-in high. Keel cross section dimensions were 0.25-in thick by 6-in high. Four lumped masses (0.138-lbf s^2/in^4 each) were added to the keel in order to make the draft of the box structure one-foot. The model's finite element mesh
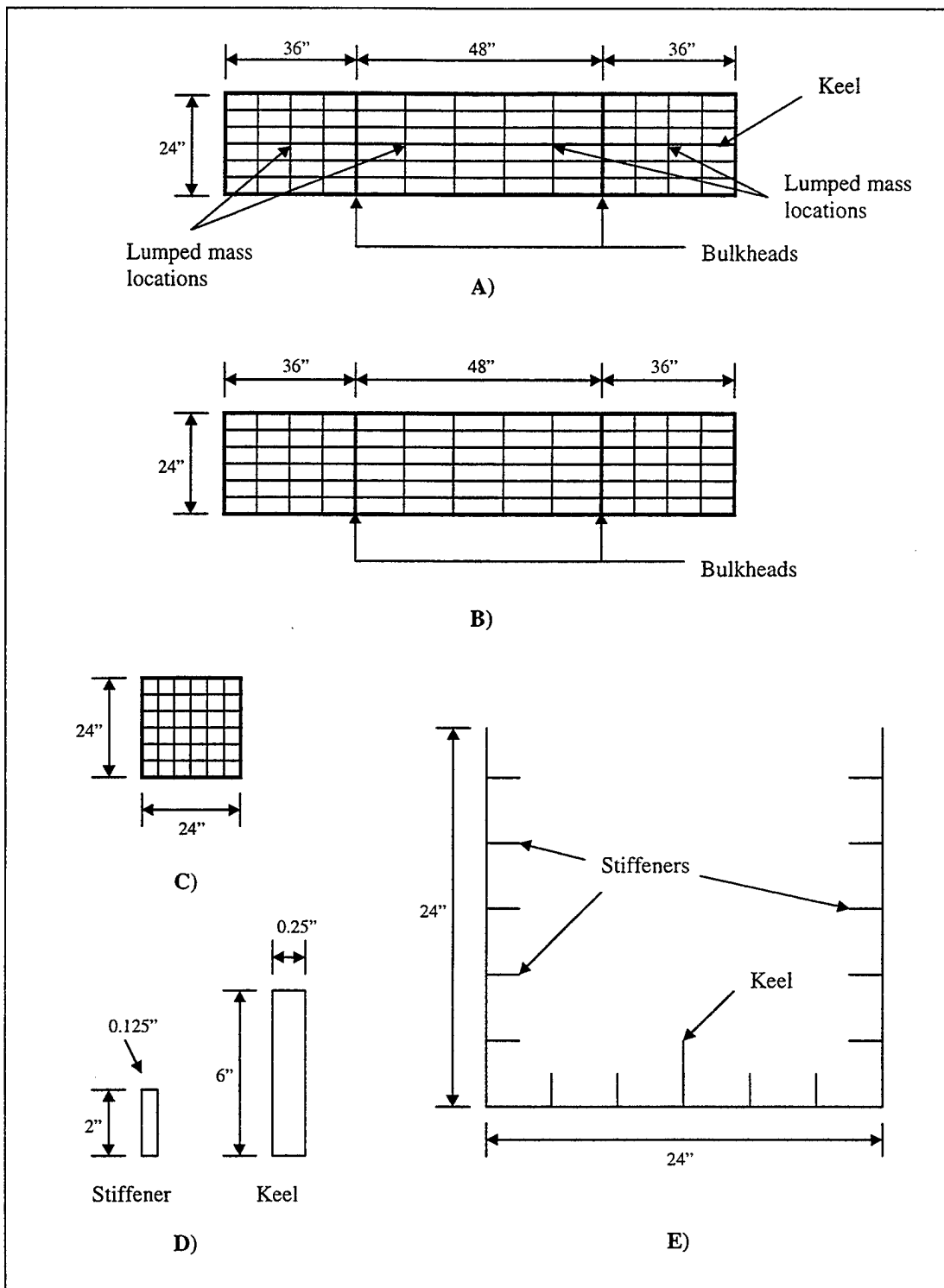
**Figure 5. Box Model Dimensions. A) Bottom B) Sides C) Ends/Bulkheads
D) Stiffener and Keel Cross Sections E) Model Cross Sections**

contained quad elements and beam elements of varying size depending on their location in the model. Quad elements on the two ends and bulkheads were 4-in by 4-in and beam elements were 4-in long. The bottom and sides of the two end compartments contained 4-in by 9-in quad elements with 4-in beam elements in the lateral direction and 9-in beam elements in the longitudinal direction. The sides and bottom of the center compartment consisted of 4-in by 9.6-in quad elements with 4-in beam elements in the lateral direction and 9.6-in elements in the longitudinal direction. In all, the box structure contained 386 nodes, 378 quad elements, 615 beam elements, and 4 point elements that were necessary for the added lumped masses. The structure finite element mesh is shown in Fig. 6 and stiffener placement is displayed in Fig. 7.

B.   SMEARING

As mentioned in the first chapter, the complexity of the box model was reduced by a process known as smearing. The density and stiffness properties of the removed elements were combined into the remaining material. In the case of a stiffened flat plate, smearing combines the elastic modulus and density of each stiffener with those of the base plate to form an equivalent orthotropic base plate. Physically, the equivalent, or smeared, plate will have the dimensions of the original base plate, Fig. 8.
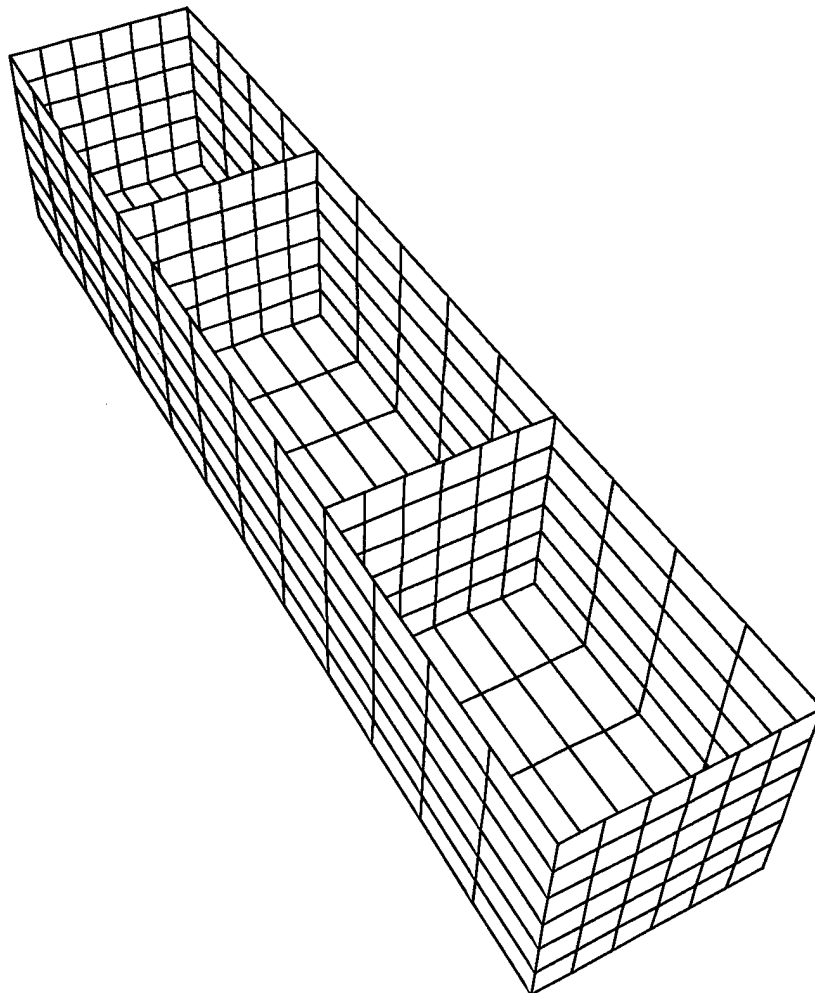
Given a stiffened, flat plate with dimensions as shown in Fig. 9, the flexural rigidity of the equivalent plate is defined in Eqs. (3.1) and (3.2) as [Ref. 10],

$$(EI)_e = (EI)_b + \sum_{i=1}^{n}(EI)_s \qquad (3.1)$$

or

$$E_e I_b = E_b I_b + \sum_{i=1}^{n}(E_s I_s / a) \qquad (3.2)$$

where $(EI)_e$, $(EI)_b$, and $(EI)_s$ are the flexural rigidities of the equivalent plate, the original base plate, and the stiffeners, respectively, and n is the number of beams smeared into the

Figure 6. Box Structure with Finite Element Mesh
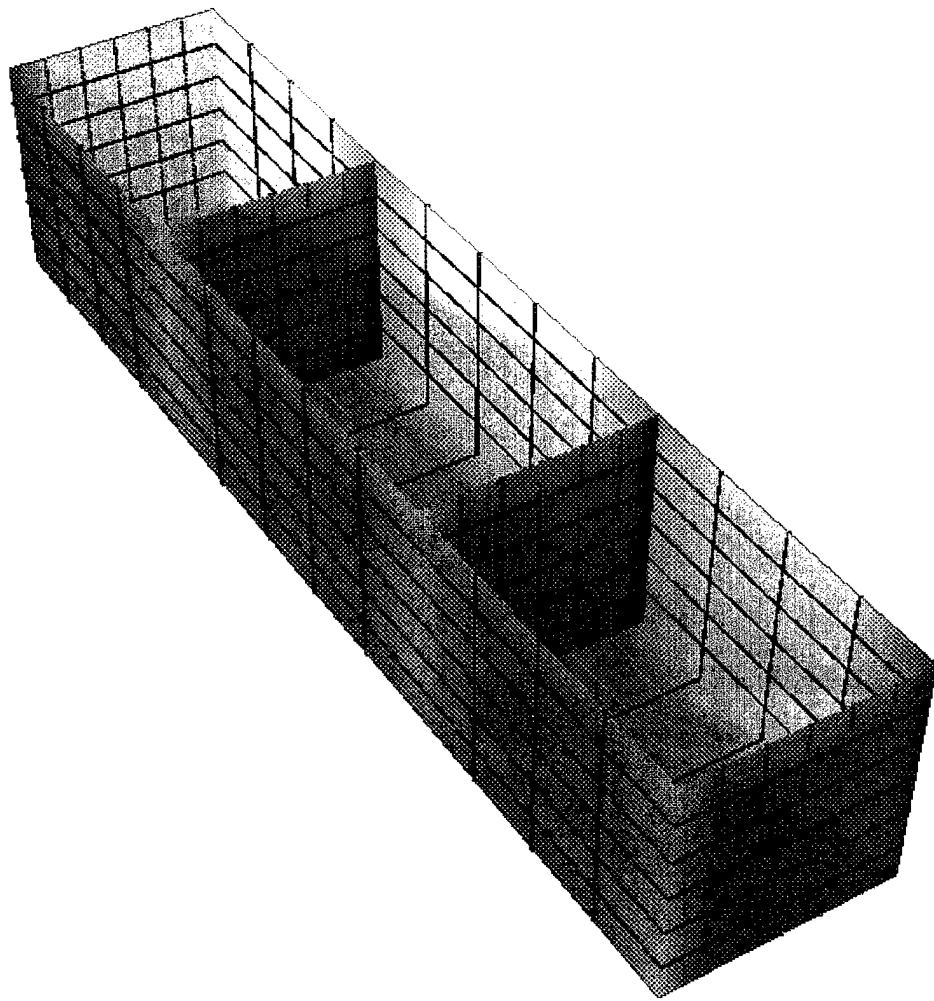
Figure 7. Stiffener Placement for the Box Structure

plate in the direction of interest. The moment of inertia of the equivalent and original base plates is $I_e = I_b$, $I_b = h_b^3/12(1-v^2)$, and the moment of inertia of a stiffener is $I_s = (b_s h_s^3/12) + b_s h_s d^2$. It then follows that the equivalent modulus of elasticity for the smeared plate is as shown in Eq. (3.3)

$$E_e = E_b + \sum_{i=1}^{n} \frac{12 E_s I_s (1 - v^2)}{a(h_b)^3} \qquad (3.3)$$

where E_e is the modulus of elasticity of the equivalent plate, E_b is the modulus of elasticity of the original base plate, E_s is the modulus of elasticity for an individual stiffener, I_s is the moment of inertia for an individual stiffener about the centroidal axis of the base plate, v is Poisson's ratio, a is the distance between stiffeners, and h_b is the thickness of the base plate. However, in this study, it was assumed that the equivalent plate thickness, h_e, is the same as the original plate thickness, h_b, and $I_e = I_b = w h_b^3/12$ where w is the width of the plate being smeared. The equivalent modulus of elasticity for the smeared plate used in this study is then defined by Eq. (3.4)

$$E_e = E_b + \sum_{i=1}^{n} \frac{E_s I_s}{I_b} \qquad (3.4)$$

Figure 8. Smearing of a Stiffened, Flat Plate

The density for the equivalent plate is defined by Eqs. (3.5) and (3.6) as follows [Ref.10],

$$\rho_e v_b = \rho_b v_b + \sum_{i=1}^{n} \rho_s v \tag{3.5}$$

and

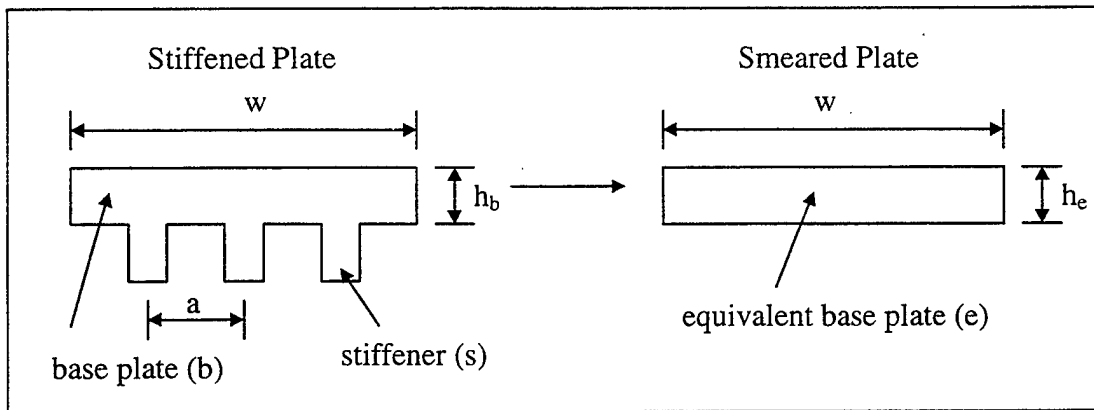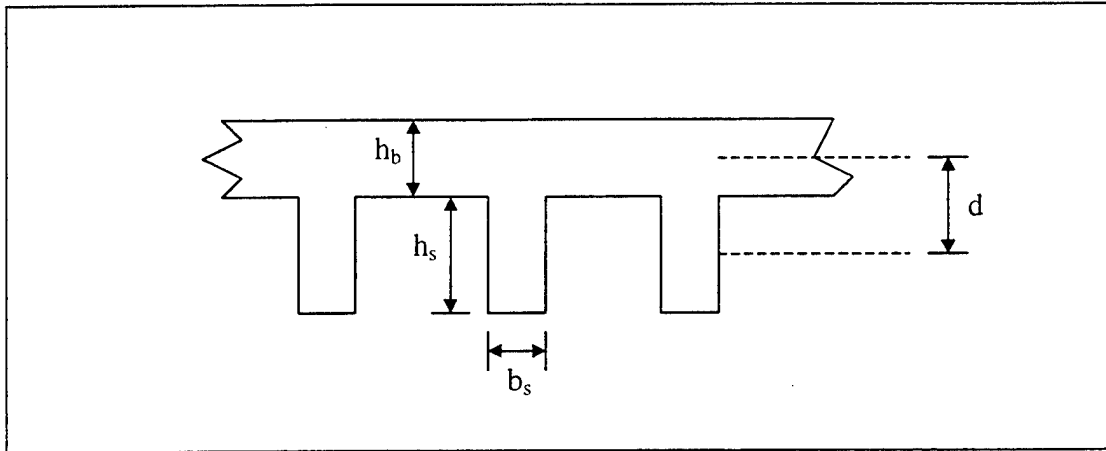$$\rho_e = \rho_b + \sum_{i=1}^{n} \frac{\rho_s v_s}{v_b} \tag{3.6}$$

where ρ_e is the density of the equivalent plate, ρ_b is the density of the base plate, ρ_s is the density of an individual stiffener, v_b is the volume of the base plate, and v_s is the volume of an individual stiffener in the direction being smeared.

Figure 9. Smeared Plate Variables

The box model was reduced twice in order to study the response of the smearing method mentioned above. A second set of models, constructed and smeared in the same manner as the first, was tested in order to study the sensitivity of the response to different keel sizes. The only differences between the two sets are the size of the keel and the size of the lumped masses required to maintain the daft of the box structure at one-foot. Keel cross section of the second model set is the same as that of the stiffeners, 0.125-in wide by 2-in high. Fig. 10 shows a cross section of the small keel model. In both model sets, the stiffeners are smeared in a locally orthotropic manner, with an equivalent elastic

modulus calculated in the longitudinal and lateral directions. For the second model set, the lumped masses were 0.1656-lbf s^2/in^4 each.
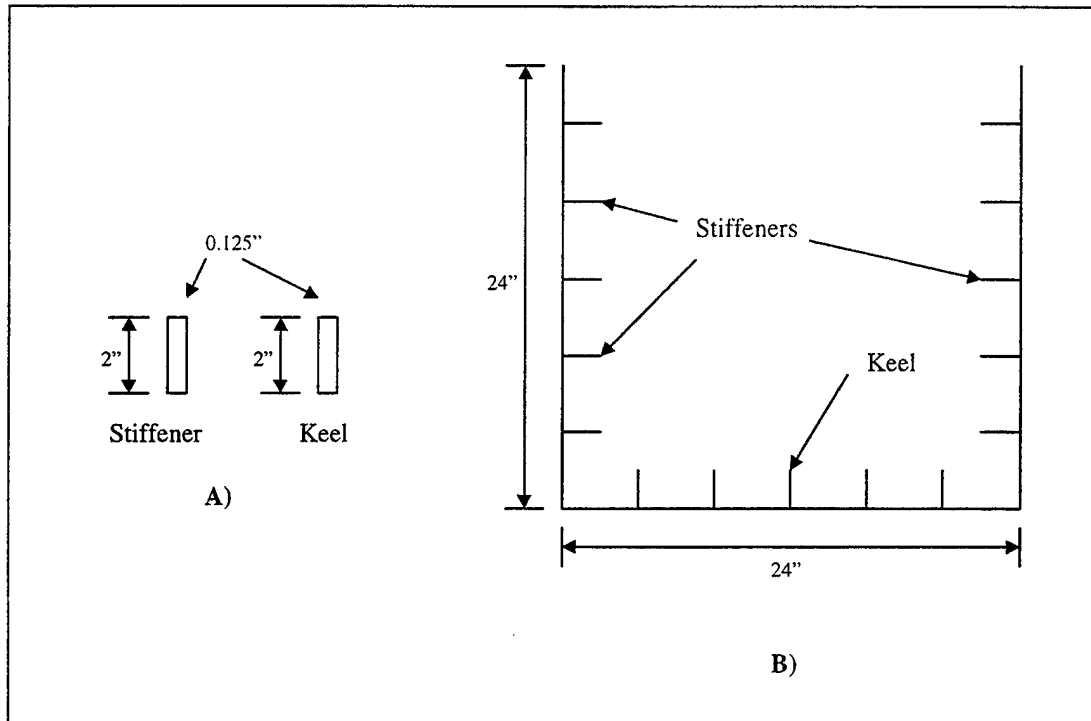

Figure 10. Small Keel Box Model Dimensions. A) Stiffener and Keel Cross Sections B) Model Cross Section

1.   First Reduction Method, Both Model Sets

In the first box model reduction, all stiffeners on the bottom were smeared into the shell plating except for the keel and all stiffeners on the sides were smeared into the shell plating except for the center longitudinal stiffeners. The bottom, sides, and ends and bulkheads were divided into smaller plates so that all stiffeners on those plates would be smeared. The reason for this was to obtain a uniform smearing in the model material by avoiding the effects from the moment of inertia of the unsmeared keel and stiffeners. The equivalent elastic moduli for the two end compartments were considered first. Due to the similar dimensions of the sides and bottom of the end compartments, each side and bottom of both end compartments was divided into two 12-in by 36-in plates, Fig. 11(A). Each plate had two 36-in longitudinally oriented stiffeners and three 12-in laterally

17

oriented stiffeners smeared into it. This results in each plate having the same longitudinal and lateral equivalent elastic modulus. Thus, the sides and bottom of both end compartments had the same equivalent elastic moduli. Similarly, the sides and bottom of the center compartment were each divided into two 12-in by 48-in plate sections, Fig. 11(B). Into each plate were smeared two 48-in longitudinally oriented stiffeners and four 12-in laterally oriented stiffeners. Since each plate was smeared in a like manner, the sides and bottom of the center compartment have the same equivalent elastic moduli.
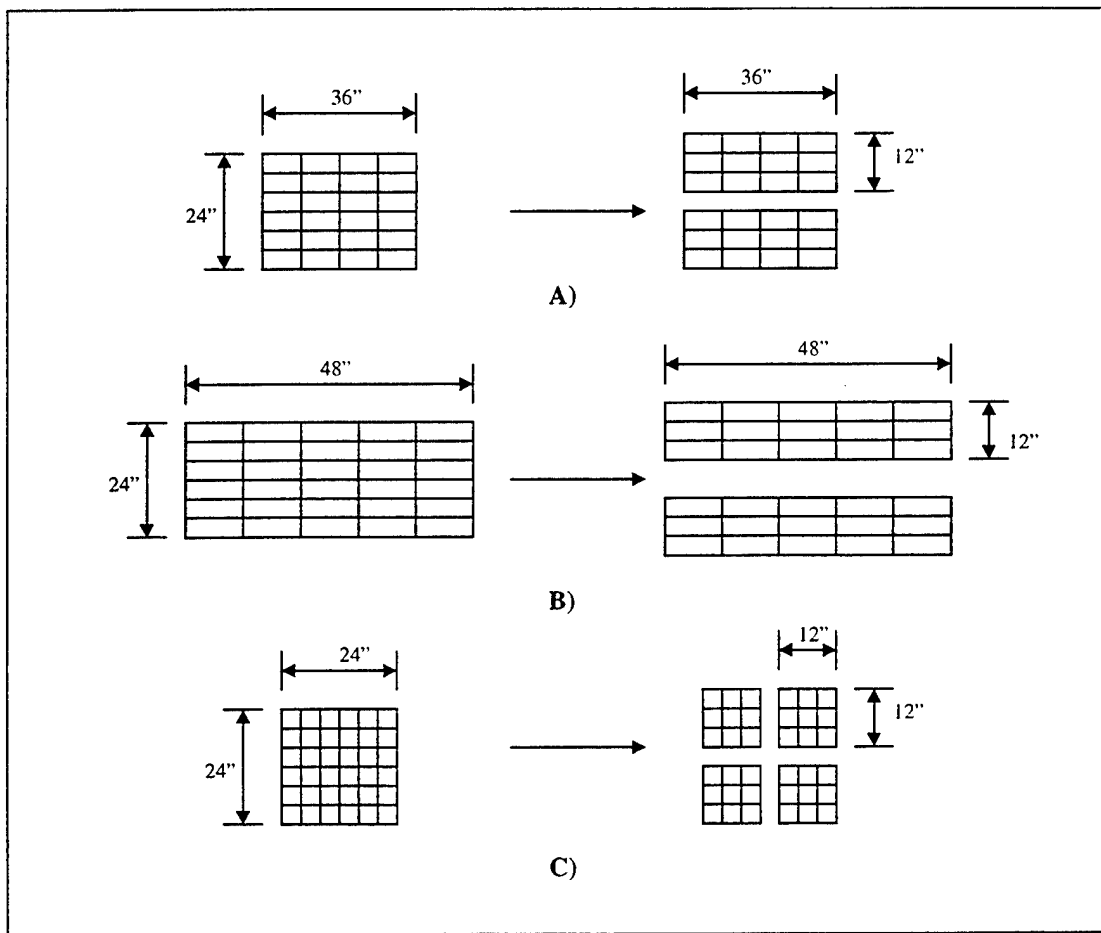

Figure 11. Smearing of Box Model Plates for the First Reduction Method.
A) Bottom and Sides of End Compartment B) Bottom and Sides of Center
Compartment C) Ends/Bulkheads

For the ends and bulkheads, all stiffeners were smeared into the shell plating except for the two center stiffeners. The equivalent elastic moduli were determined by

dividing each end and bulkhead into four 12-in square plates, Fig. 11(C). On each plate, two 12-in stiffeners were smeared in both the longitudinal and lateral directions. By geometry, the four 12-in square plates had the same equivalent elastic moduli in each direction. It then followed that each end and bulkhead had the same equivalent elastic modulus. The stiffener smearing for the first reduction of the box structure is shown in Fig. 12.

Equivalent mass densities for the box structure were calculated in a similar manner by dividing the compartments, ends, and bulkheads into smaller plates. The equivalent density of each plate was determined by the product of the density and volume of each stiffener on the plate divided by the volume of the plate as described above. This
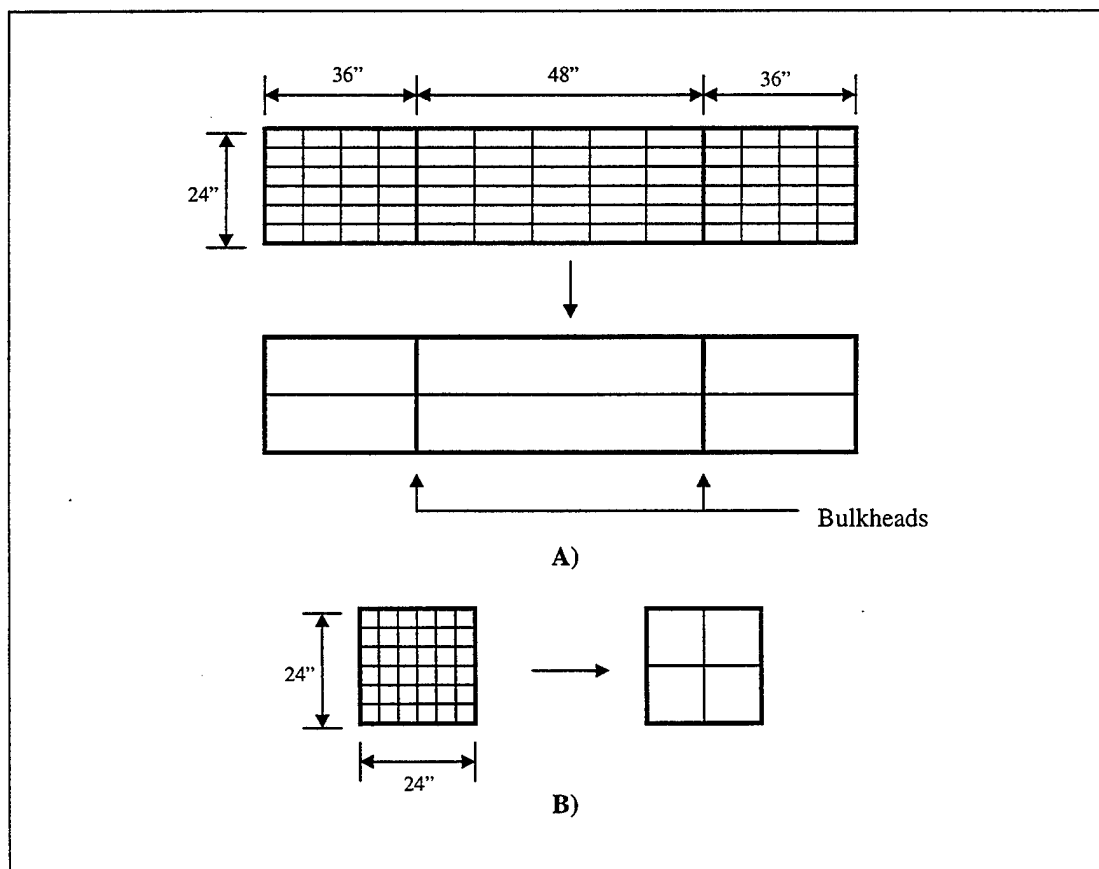
Figure 12. The First Reduction Method. A) Stiffener Smearing on the Sides and Bottom B) Stiffener Smearing on the Ends and Bulkheads

value was added to the original plate density, yielding the equivalent plate density. Since the only difference between the model sets was the unsmeared keel, the equivalent elastic moduli and densities for both first reduction models were be the same. Table 1 lists the equivalent elastic moduli and mass density values for the first reduction of the box models. Fig. 13 shows stiffener location for the first model reduction. The different colors of the figure denote sections of the model with the same elastic modulus and density. As a result of smearing the stiffeners, the first reduction models have 87 beam elements but still have 386 nodes and 378 quad elements.

|	Fore/Aft Compartment Bottom and Sides	Center Compartment Bottom and Sides	Ends/Bulkheads
E_{long} or E_x (psi)	1,564,848,000	1,564,848,000	1,564,848,000
E_{lat} or E_y (psi)	797,424,000	797,424,000	1,564,848,000
ρ (lbf s^2/in^4)	0.0009187	0.0009187	0.0009799

Table 1. Equivalent Elastic Moduli and Mass Densities for the First Reduction Method, Both Model Sets

2.   Second Reduction Method, Both Model Sets

For the second box model reduction, all stiffeners on the model except for the keel were smeared into the shell plating. Considering the sides of the two end compartments, stiffeners on the entire 24-in by 36-in plate were smeared in order to calculate the equivalent elastic moduli, Fig. 14(A). This includes five 36-in longitudinally oriented stiffeners and three 24-in laterally oriented stiffeners. The bottom of the end compartments was smeared in the same manner as the first reduction model by dividing it into two 12-in by 36-in plates, Fig. 14(B). The equivalent elastic moduli of the center compartment were determined by considering the sides and the bottom separately, Fig. 14(C) and (D), respectively. All stiffeners on the 24-in by 48-in side plates, five 48-in longitudinally oriented stiffeners and four 24-in laterally oriented stiffeners were smeared. The bottom of the center compartment was smeared like the bottom of the end compartments by using the 12-in by 48-in plates in the calculations. The equivalent elastic moduli for the ends and bulkheads were calculated using the 24-in square plate section for smearing with five 24-in stiffeners in the longitudinal and lateral
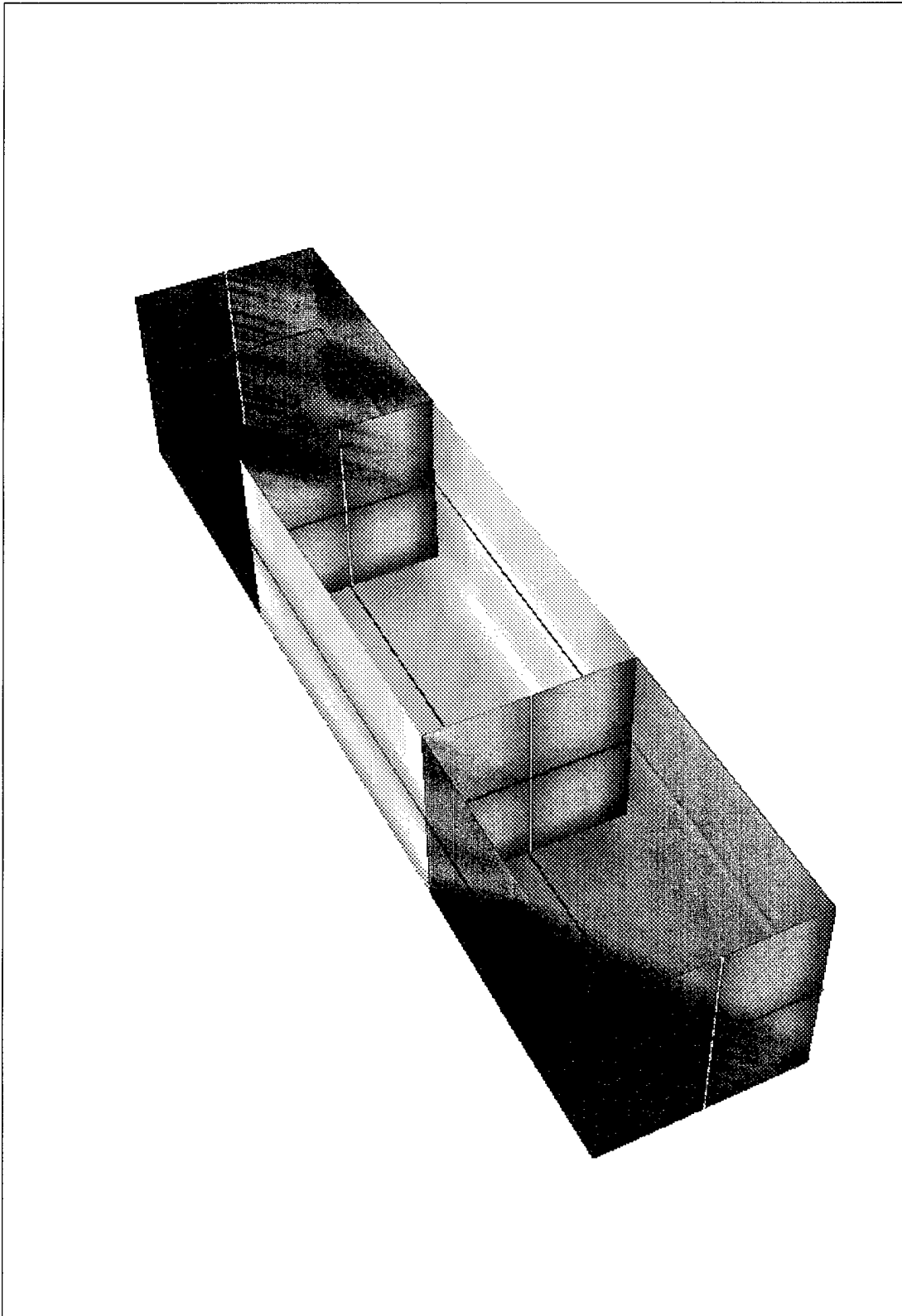
Figure 13. Stiffener Placement for the First Model Reduction
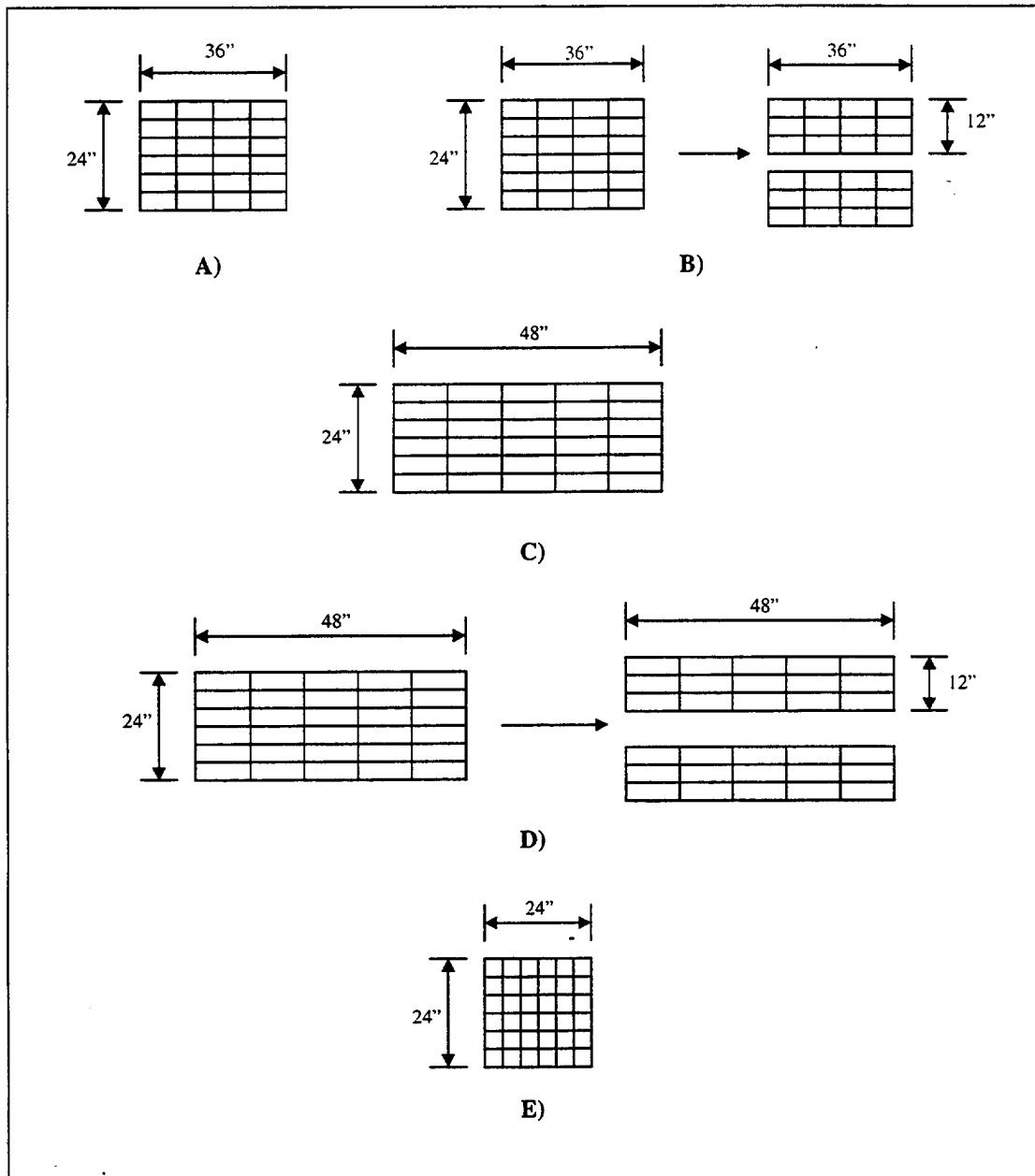
Figure 14. Smearing of the Box Model Plates for the Second Reduction Method.
A) Sides of the End Compartments B) Bottom of the End Compartments
B) Sides of the Center Compartment D) Bottom of the End Compartment
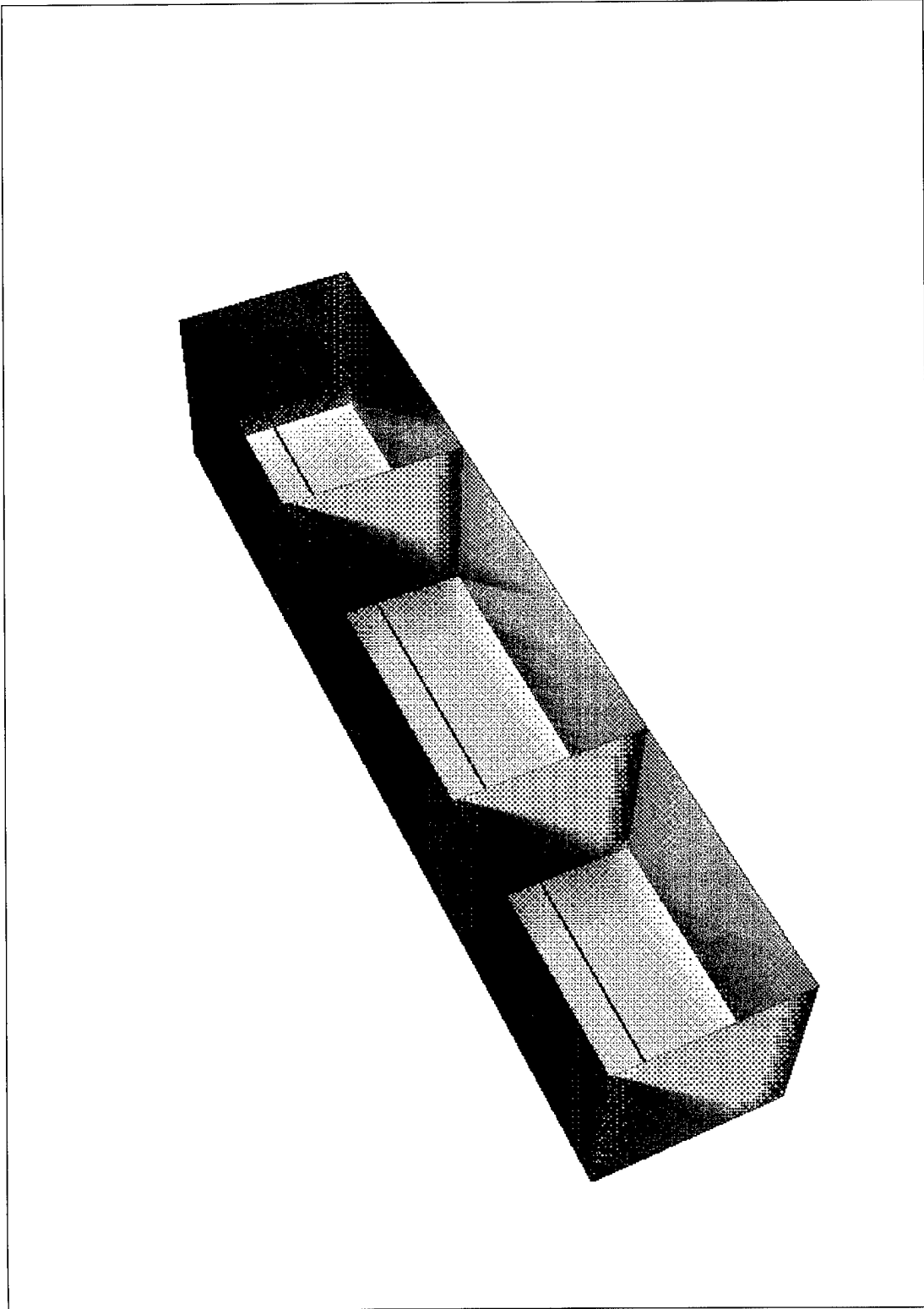E) Ends/Bulkheads

directions, Fig. 14(E). The stiffener smearing for the second reduction of the box structure is shown in Fig. 15 and stiffener location is shown in Fig. 16.

The equivalent mass densities were determined in a similar manner by dividing the compartments, ends, and bulkheads into smaller plates. As with the first reduction, the equivalent density of each plate was determined by adding the original plate density to the product of the density and volume of each stiffener on the plate divided by the volume of the plate. Like the first reduction, equivalent elastic moduli and densities for both second reduction models will be the same. The different colors of the figure denote sections of the model with the same elastic modulus and density. Table 2 lists the equivalent elastic moduli and mass density values for the second reduction of the box models. As a result of the second reduction method, these models had 13 beam elements but still had 386 nodes and 378 quad elements.
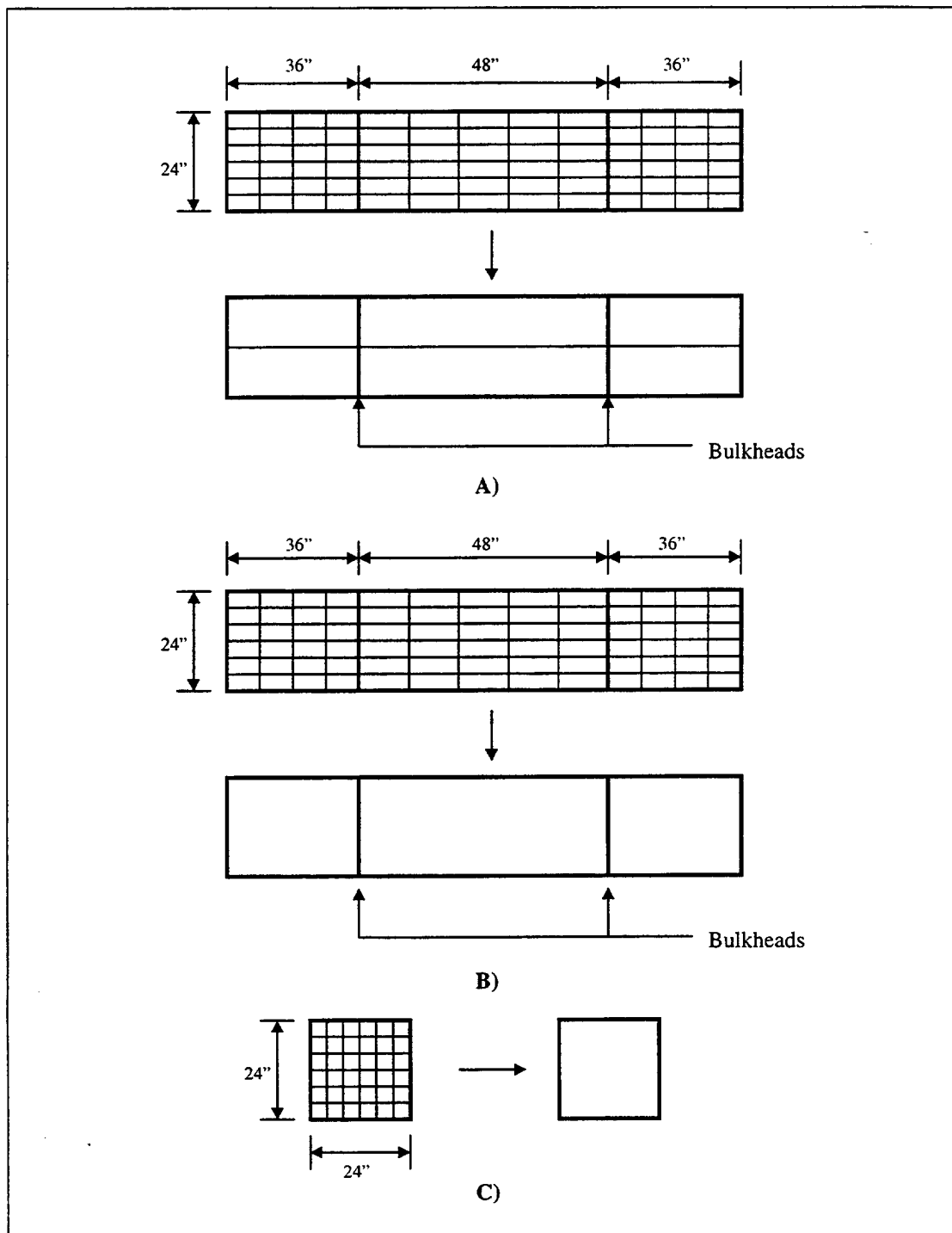
Figure 15. The Second Reduction Method. A) Smearing on the Bottom B) Smearing on the Sides C) Smearing on the Ends/Bulkheads

Figure 16. Stiffener Location for the Second Model Reduction

	Fore/Aft/Center Compartment Bottom	Fore/Aft/Center Compartment Sides	Ends/Bulkheads
E_{long} or E_x (psi)	1,564,848,000	1,948,560,000	1,948,560,000
E_{lat} or E_y (psi)	797,424,000	797,424,000	1,948,560,000
ρ (lbf s^2/in^4)	0.0009187	0.0009494	0.0010410

Table 2. Equivalent Elastic Moduli and Mass Densities for the Second Reduction Method, Both Model Sets

IV. TEST DESCRIPTION AND RESULTS

A. TEST DESCRIPTION

All six box structures were subjected to the same shock test. A 20-lb spherical charge of HBX-1 was detonated amidships on the starboard (right) side abeam of the model at a horizontal range of 8.37 ft and depth of 15.5 ft for a resulting range of 16.75 ft as seen in Fig. 17.
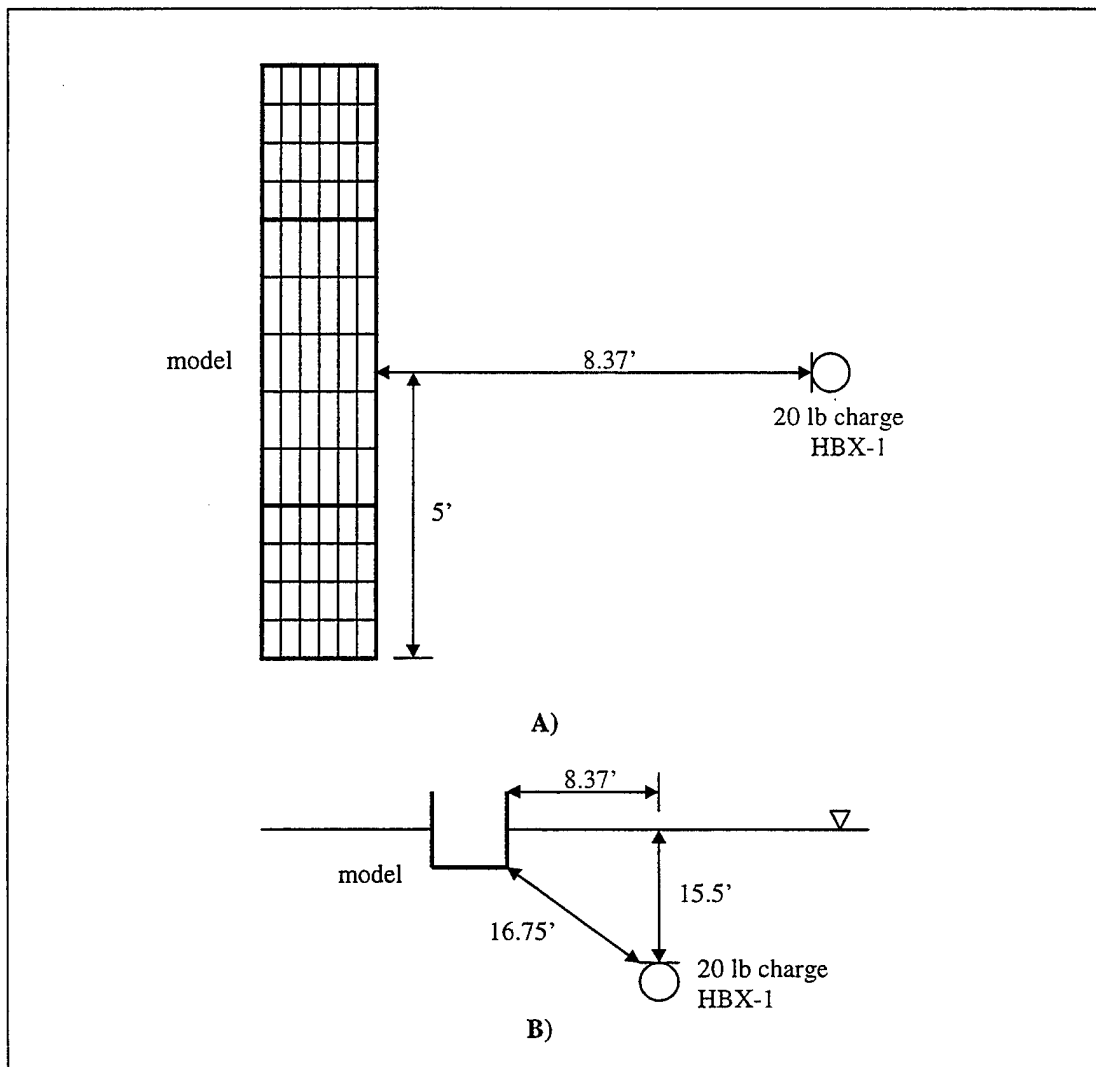
**Figure 17. Shock Test Geometry. A) Top View B) Cross Section View**

B. RESULTS

Several different nodes throughout the after half of the box model were chosen in order to study the overall response trends of the keel, sides, and bulkheads to the shock test, as seen in Fig. 18. Seven nodes were selected for examination and represent the same location on each of the six models tested. Since the explosive charge was detonated at the longitudinal center of the model, the nodal responses of the forward half of the structure will be the same as those of the after half due to symmetry of the model.

A time step of 1×10^{-6} seconds was used in the USA/LS-DYNA analysis. This time step, based on a characteristic length taken from the longest side of the quadrilateral elements, was computed using LS-DYNA. The node responses were recorded at an interval of 1×10^{-5} seconds for 3,000 time steps, representing a total time of 30 milliseconds. The velocity profiles are shown out to 15 milliseconds in order to study the initial velocity responses of the models clearly.

1. Large Keel Model Results

Velocity responses of the large keel models are displayed in Figs. 19 – 25. The velocity profile for node 55 (see Fig. 18 for location) is shown in Fig. 19. Peak athwartships velocity of the full-unsmeared model, 255.42 in/sec, was much greater than the first and second reduced models, 68.46 in/sec and 86.94 in/sec, respectively. The peak resultant velocity responses of the reduced models, 194.47 in/sec for the first reduction and 206.11 for the second reduction, were significantly less than that of the full model, 264.97 in/sec. It would be expected that the reduced model velocity profiles would have greater peak values than those of the full model since the reduced models have fewer stiffeners than the full model and are thus not as rigid. In this particular case, though, the opposite result has occurred. As can also be seen, velocities of the reduced models did not oscillate as much as compared to the full model.

The athwartships velocity profile for node 66 (see Fig. 18 for location), as seen in Fig. 20, shows peaks that were closer in value between the full model and reduced models than was the case for node 55, but were still considerably different. The full
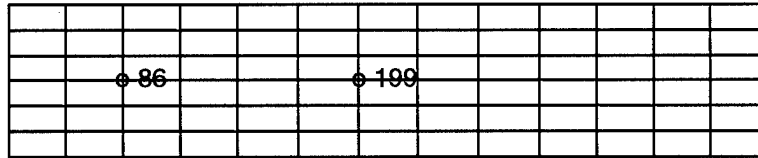
A)
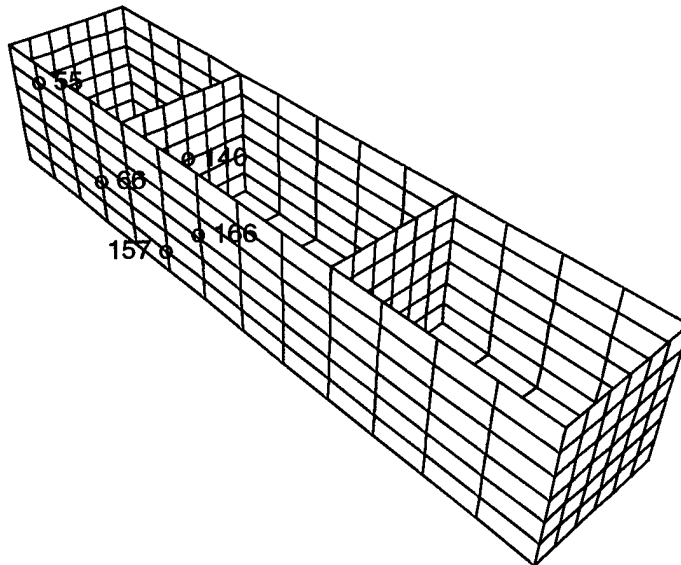
B)

**Figure 18. Node Locations for the Shock Test. A) Keel Nodes
B) Side and Bulkhead Nodes**

model had a peak velocity of 393.09 in/sec while the first and second reductions had 453.07 in/sec and 444.58 in/sec, respectively. Peak values differences for the resultant velocity were slightly greater with the full model at a peak velocity of 393.38 in/sec and the first and second reductions at 480.59 in/sec and 472.39 in/sec, respectively. Both the full and reduced models responded in the expected manner. The reduced models had greater peak velocities than the full model as a result of having a fewer number of stiffeners through out the model, making it less stiff than the full model. Like node 55, these responses of the reduced models did not oscillate as much as those of the full model. It can be seen that the athwartships and resultant velocities began to converge near the same values for all three models, 9 in/sec for the athwartships velocity and 38 in/sec for the resultant velocity. Also of note, node 66 of the full model had greater peak velocities than node 55, but oscillated less freely than node 55. This was due to the fact that node 66 has more structural support from the nearby bottom and after bulkhead than node 55, which is located closer to the top of the structure's side, as seen in Fig. 18.

The velocity profiles of keel node 86, shown in Fig. 21, had significantly different peak values between the full model and reduced models. Peak vertical velocity of the full model was 88.14 in/sec while peak velocity of the first and second reductions were 209.88 in/sec and 213.10 in/sec, respectively. It would be expected that the keel node of the full model would exhibit a positive initial vertical velocity. However, the vertical velocity for node 86 became negative initially, then became positive. Thus, in this particular testing case, the keel of the full model deformed in the negative direction before deforming in the positive direction. Both reduced models displayed a similar behavior that was much less pronounced. The large difference in peak resultant velocities is also seen in the velocity profile of node 86. The full model had a peak resultant velocity of 110.80 in/sec while the first and second reduction models had peak velocities of 210.17 in/sec and 213.32 in/sec, respectively. Again, the models responded in the expected manner with the reduced models having greater peak velocities than the full model. It can be noted that the full and reduction model velocities quickly converged to similar values of approximately 32 in/sec for the vertical velocity and 36 in/sec for the resultant velocity.

The after bulkhead velocity profiles for node 140 are displayed in Fig. 22. The peak velocity for the full model in the longitudinal direction was much greater than the peak velocities of the reduced models. In addition, the full model velocity response oscillated with greater amplitude than the reduced models. Peak longitudinal velocity for the full model was 88.55 in/sec while peak velocities for the first and second reduced models were 5.34 in/sec and 9.20 in/sec, respectively. In contrast, the peak resultant velocities for the reduced models, 267.56 in/sec for the first reduction and 266.26 in/sec for the second reduction, were much greater than that of the full model, 122.46 in/sec. The resultant velocity profiles show the expected results with the reduced model peak responses greater than that of the full model. However, the longitudinal responses did not show the expected behavior. The resultant velocities of both reduced models quickly converged near similar values of 35 in/sec.

Node 157, located on the starboard side of the center compartment as seen in Fig. 18, experienced higher peak velocities in the reduced models than in the full model, as shown in Fig. 23. The first reduction model had a peak athwartships velocity of 608.40 in/sec and the second reduction model had a peak athwartships velocity of 593.49 in/sec. Peak athwartships velocity for the full model was 344.99 in/sec. Resultant velocity responses were similar. The first reduction model had a peak resultant velocity of 626.67 in/sec and the second reduction had a peak resultant velocity of 612.35 in/sec while the full model had a peak resultant velocity of 346.19 in/sec. Here, the models responded in the expected manner with the reduced models having greater peak velocities than the full model. The full model and both reduced models converged to approximately the same athwartships and resultant velocities, 17 in/sec and 35 in/sec, respectively. As can be seen, velocities in the reduced models did not oscillate as did those in the full model.

Node 166 on the starboard side, center compartment showed behavior similar to that of node 55. The velocity responses are displayed in Fig. 24. The full model peak athwartships and resultant velocities were greater than both reduced models. In addition, the full model displayed more oscillation than did the reduced models. The peak athwartship velocity for the full model was 333.47 in/sec while the peak athwartships velocities for the first and second reduction models were 222.35 in/sec and 249.86 in/sec,

respectively. The resultant velocity for the full model was 333.72 in/sec and the resultant velocities for the first and second reduction models were 248.11 in/sec and 272.39 in/sec, respectively. For node 166, the reduced models did not respond in the expected manner. As is seen, the reduced model peak velocities were less than the peak value for the full model. Again, velocities for all models in both profiles converged near similar values, 12 in/sec for the athwartships velocity and 35 in/sec for the resultant velocity. As with the comparison between node 55 and 66, node 157 of the full model had greater peak velocities than node 166, but oscillated less freely than node 166. This was due to the fact that node 157 has more structural support from the nearby bottom and after bulkhead than node 166, as was the case with nodes 55 and 66.

The velocity profiles for keel node 199, shown in Fig. 25, show large differences in the peak velocities between the full model and reduced models. The peak vertical velocities for the first and second reduction models were, respectively, 321.22 in/sec and 321.94 in/sec. The peak vertical velocity for the full model was 126.01 in/sec. Like node 86, the vertical velocity of the full model initially became negative before becoming positive. The reason is due to the initial downward motion of the keel as described for node 86. A large difference between the responses is seen in the resultant velocity profile as well. The first and second reduction models had peak resultant velocities of 326.65 in/sec and 327.53 in/sec, respectively, while the full model had a peak resultant velocity of 151.19 in/sec. It can be seen that the reduced model peak velocities were greater than that of the full model, as expected. Velocities for both profiles converged near similar values of 30 in/sec for the vertical velocity and 35 in/sec for the resultant velocity. Tables 3 and 4 list the peak velocity responses for the large keel model set.

2. Small Keel Model Results

The small keel model set was tested to determine the sensitivity of the velocity responses to different keel sizes. Overall, velocity response profiles for the small keel models, shown in Figs. 26 – 32, were similar to those of the large keel models.

The peak athwartship velocity for node 55 of the full model, 254.16 in/sec as seen in Fig. 26, was much greater than those of the first and second reduction models, 69.99 in/sec, and 89.08 in/sec, respectively. The resultant peak velocities were somewhat closer in value with the full model at 260.08 in/sec and the first and second reduction models at 226.15 in/sec and 234.43 in/sec, respectively. As with the large keel model set, the reduced models have smaller peak velocities and show much less oscillation than the full model.

The velocity profiles of node 66 are shown in Fig. 27. Results of the small keel model set were again similar to those of the large keel model. In the athwartships direction, the first reduction had a peak velocity of 454.58 in/sec and the second reduction had a peak velocity of 446.10 in/sec while the full model had a peak velocity of 392.45 in/sec. The resultant velocity profile shows a slight increase in the difference between peak velocity values. Peak velocities for the first and second reduction models were, respectively, 482.86 in/sec and 474.57 in/sec, and the full model had a peak resultant velocity of 392.69 in/sec. Peak velocity behavior is the same as that for node 66 on the large keel model. The full and reduced model velocities began to converge to similar velocity values, approximately 10 in/sec for the vertical component and 33 in/sec for the resultant velocity. Comparing the response of node 55 to node 66, node 66 oscillated much less than node 55 as a result of more structural support from the bottom and after bulkhead nearby. This same observation was made for the large keel model set.

Fig. 28 displays the velocity profiles for keel node 86. Overall, the peak responses were less than those of the large keel model set. A significant difference in peak vertical velocities still exists between the full and reduced models, though. The full model had a peak value of 76.88 in/sec while the first and second reduction models had values of 131.19 in/sec and 131.07 in/sec, respectively. Another similarity between the large and small keel model sets was the initial negative velocity values for node 86 on all three models. Peak resultant velocities are in somewhat closer agreement with the full model having a peak of 102.50 in/sec, and the first and second reduction models having peaks of 132.31 in/sec and 132.37 in/sec, respectively. As expected, the reduced models had greater peak velocities than the full model. Full and reduced model velocities in both

vertical and resultant velocity profiles converged to similar values, approximately 32 in/sec for the vertical velocities and approximately 35 in/sec for the resultant velocities. These values are very similar to the values of the large keel set.

The velocity profiles of the after bulkhead node, node 140, shown in Fig. 29, show large oscillations and similar peak velocity responses as was the case in the large keel models. However, peak velocities in the small keel models were more varied than in the large keel model set. Peak velocity for the full model in the longitudinal direction was 48.80 in/sec, which is less than that of the large keel model. The fore and aft peak velocity for the first reduction model was 26.19 in/sec, a value greater than the large keel model (5.342 in/sec). The second reduction model displayed a peak resultant velocity of 9.39 in/sec, a value almost identical to that of the large keel model (9.21 in/sec). The reduced models show a greater peak resultant velocity than the full model. The peak resultant velocities for the first and second reduction models were 225.98 in/sec and 226.54 in/sec, respectively while the full model peaked at a velocity of 131.33 in/sec. The resultant velocities converged near similar values of 35 in/sec. As compared to the large keel model set, the full model peak resultant velocity for the small keel was more than that for the large keel, while both reduced small keel model resultant velocities were somewhat smaller than those of the large keel models.

The athwartships and resultant velocity profiles for starboard side node 157, as shown in Fig. 30, are similar to those of the large keel model set. Peak athwartships velocities for the reduced models were 604.76 in/sec for the fist reduction model and 589.75 in/sec for the second reduction model. The peak athwartships velocity for the full model was 350.13 in/sec. Resultant velocity responses show a peak for the first reduction model of 623.05 in/sec and a peak for the second reduction model of 608.67 in/sec. The full model reached a peak velocity of 351.27 in/sec. Here, the models responded in the expected manner, with the reduced models having greater peak velocities than the full model. Velocity values converged near 14 in/sec for the athwartships velocity and near 35 in/sec for the resultant velocity. Similar to the large keel model set, the velocity responses of the reduced models did not oscillate as much as those of the full model.

Velocity profiles for node 166, shown in Fig. 31, are also very similar to the large keel responses. The full model peak athwartships and resultant velocities were greater than those of both reduced models. Additionally, the full model showed more oscillation than did the reduced models. The peak athwartships velocity for the full model was 331.91 in/sec while the peak athwartships velocities for the first and second reduction models were 222.37 in/sec and 249.97 in/sec, respectively. Resultant velocity profiles show the full model peak velocity of 332.10 in/sec, while those of the first and second reduction models were 248.55 in/sec and 272.84 in/sec, respectively. Similar to the large keel model set, the reduced models did not respond as expected, having peak velocities less than that of the full model. The velocities for all models again converged near similar values, 12 in/sec for the athwartships velocity and 37 in/sec for the resultant velocity. These values are very close to those found on the large keel models. As explained for the large keel model, node 166 of the full model oscillated more freely than did node 157.

Peak velocity values for node 199 on the small keel model, shown in Fig. 32, were greater than those of the large keel model set. The peak vertical components of the first and second reduction models were 478.38 in/sec and 479.01 in/sec, respectively, while the peak vertical velocity of the full model was 176.16 in/sec. In comparing this full model node to the same in the full model with the large keel, the initial vertical velocity again became negative before becoming positive. The resultant velocities for the small keel models were greater than those of the large keel models. The peak resultant velocities for the first and second reduction models were 482.94 in/sec and 483.65 in/sec, respectively, while the peak resultant velocity for the full model was 212.23 in/sec. As with the large keel model, the reduced model peak velocities were much greater than the peak velocity of the full model. Velocities for both profiles converged near similar values of 33 in/sec for the vertical velocity and 35 in/sec for the resultant velocity. These results are, again, similar to the large keel model set. Tables 5 and 6 list the peak velocity responses for the small keel model set.

The results obtained from smearing the large keel model were varied. For the nodes chosen on this model set, peak velocities between the full model and the reduction

35

models were significantly different. Nodes 55, 140, and 166 did not show the expected results with regards to the reduced models. These three nodes on the reduced models had peak velocities that were less than the peak velocity of the full model. In addition, the side nodes of the full model, nodes 55, 66, 157, and 166 as seen in Fig. 18, oscillated with greater amplitude than those nodes on the reduced models. This behavior was also observed in the response of node 140. Keel node responses of the reduced models (nodes 86 and 199) show major differences in velocity profiles as well. As can be seen from these velocity profiles, smearing seems to have a dampening effect on the velocity responses in this particular case. One interesting note is that in most of the responses discussed, the first and second reduction models had very similar peak velocity values and profile shapes.

As for keel sensitivity, it was noted that most response curves for the small keel models were very similar in peak value and shape as those of the large keel models. Like the large keel model set, nodes 55, 140, and 166 did not show the expected results of the reduced models, having greater peak velocities than that of the full model. There were significant differences between the keel and bulkhead responses of the large keel and small keel models. The velocity response of node 86 on the small keel model was less sensitive than the large keel model, having smaller peak velocity values than those on the large keel model. Keel node 199 showed different behavior. Node 199 on the small keel model was more sensitive than the large keel model and displayed greater peak values than those on the large keel model. Node 140 displayed different sensitivity behaviors. The full model showed a less sensitive longitudinal velocity response while the first reduction showed greater sensitivity. The sensitivity of node 140 on the second reduction model was unchanged. Conversely, the full model showed more sensitivity in the resultant velocity while both reduction models were less sensitive. Like the large keel set, most responses of both reduction models were similar in peak velocity value and shape.

Node 55 Velocity
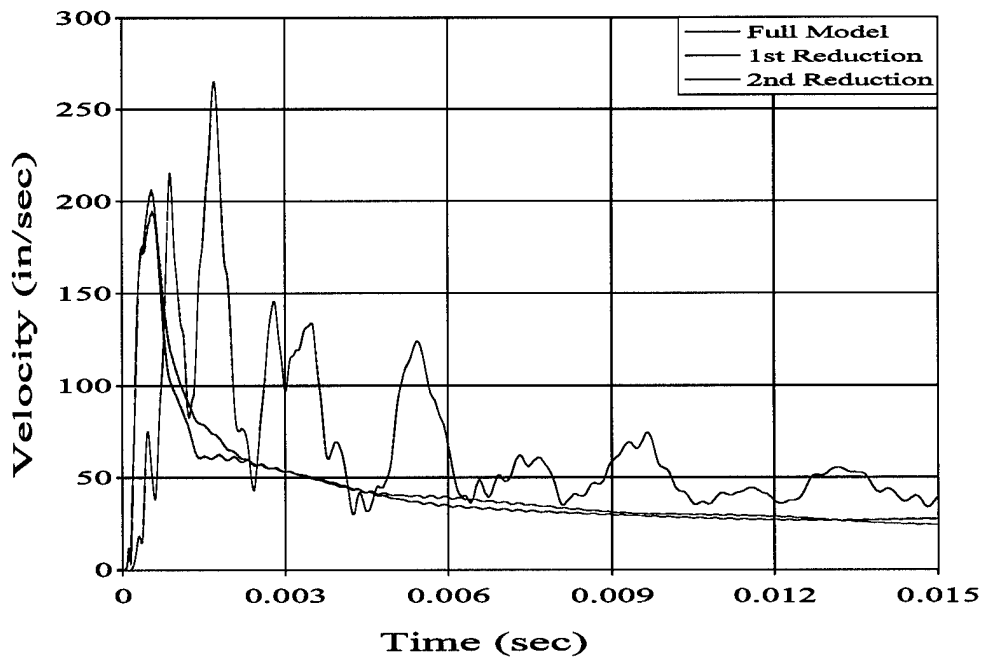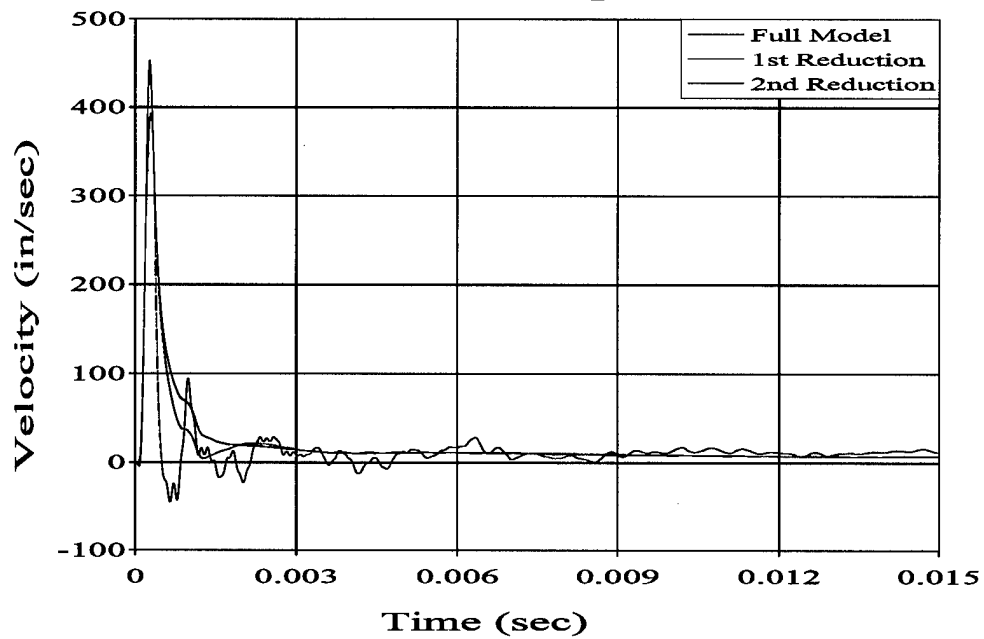
Athwartships
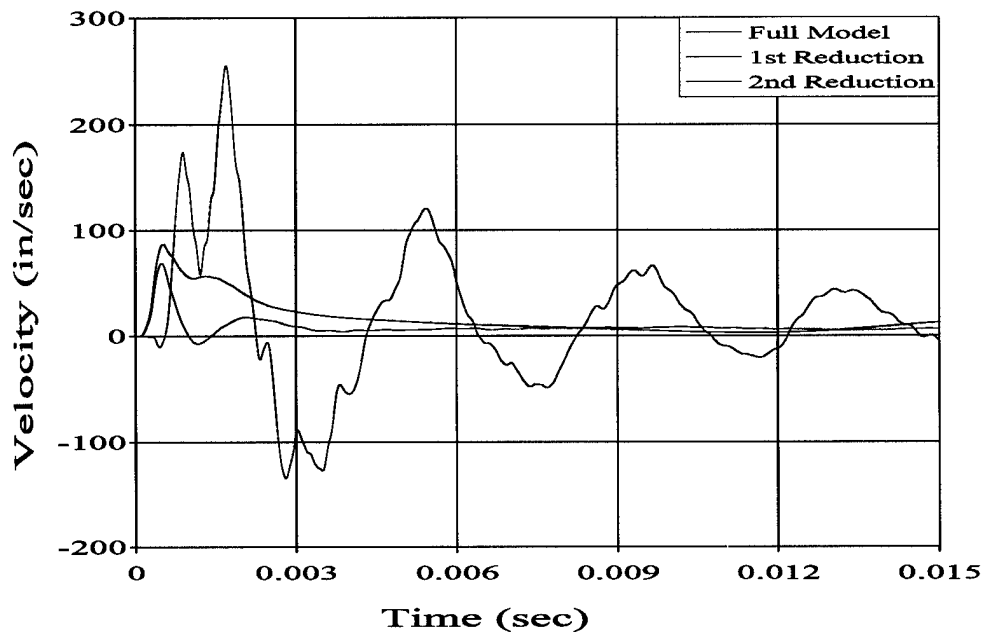
Node 55 Resultant Velocity

Figure 19. Large Keel Model, Node 55 Velocity Profiles

37

Node 66 Velocity
Athwartships
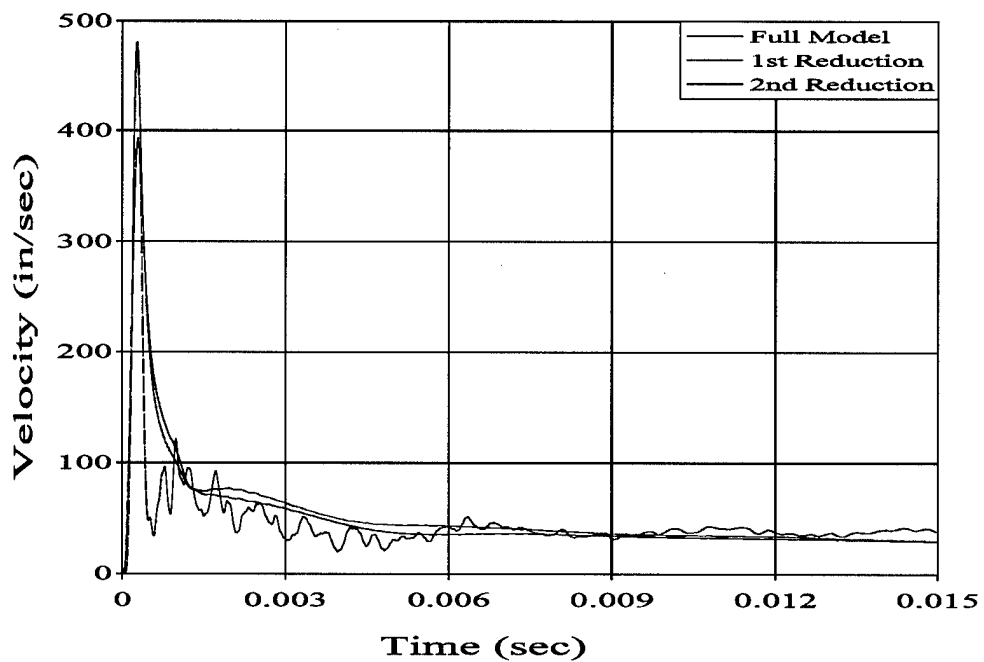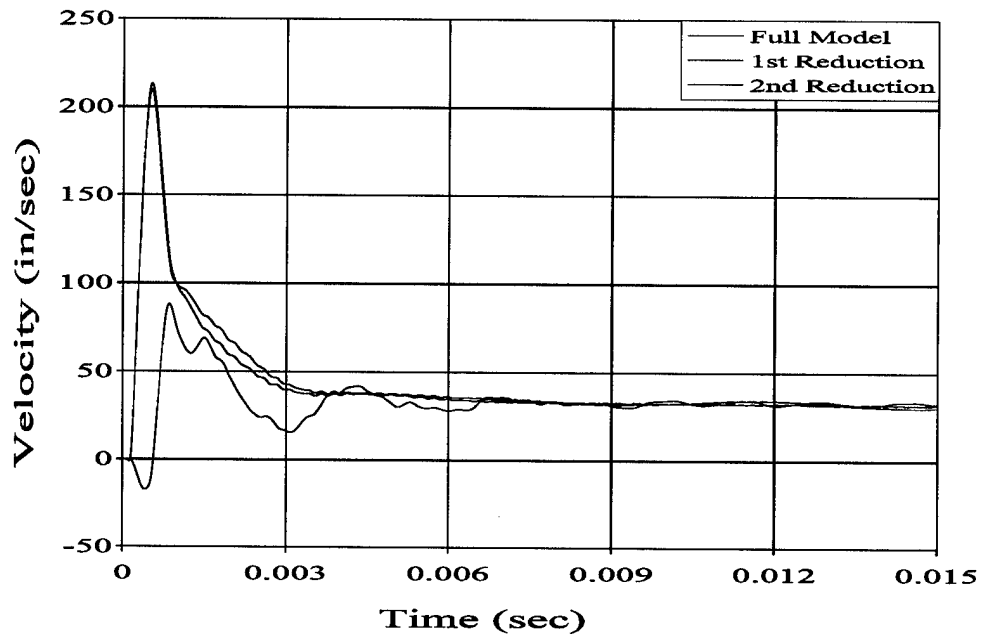

Node 66 Resultant Velocity

Figure 20. Large Keel Model, Node 66 Velocity Profiles

38

Node 86 Velocity
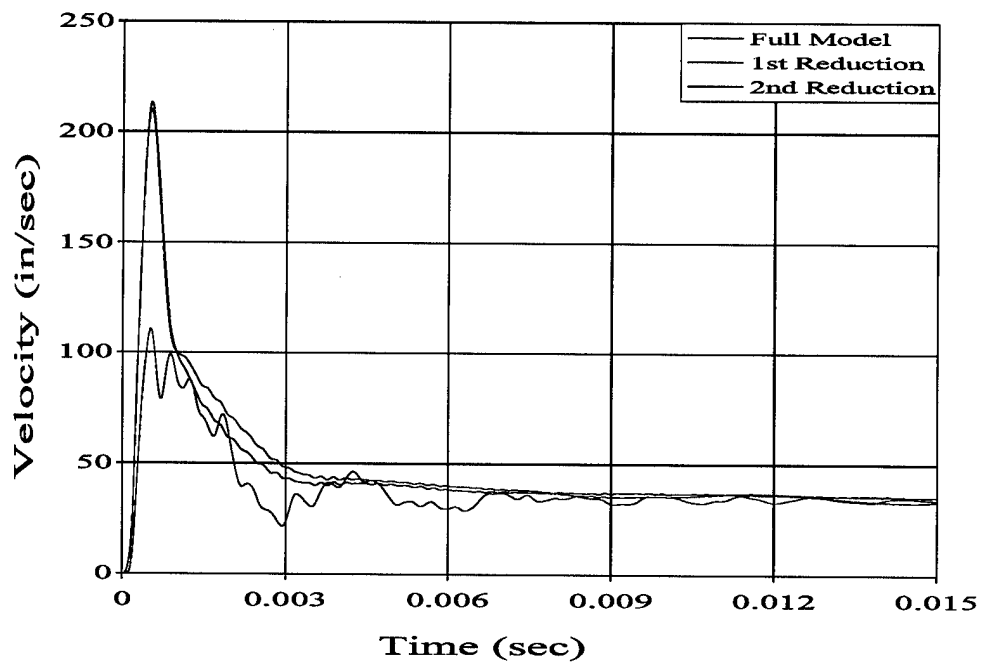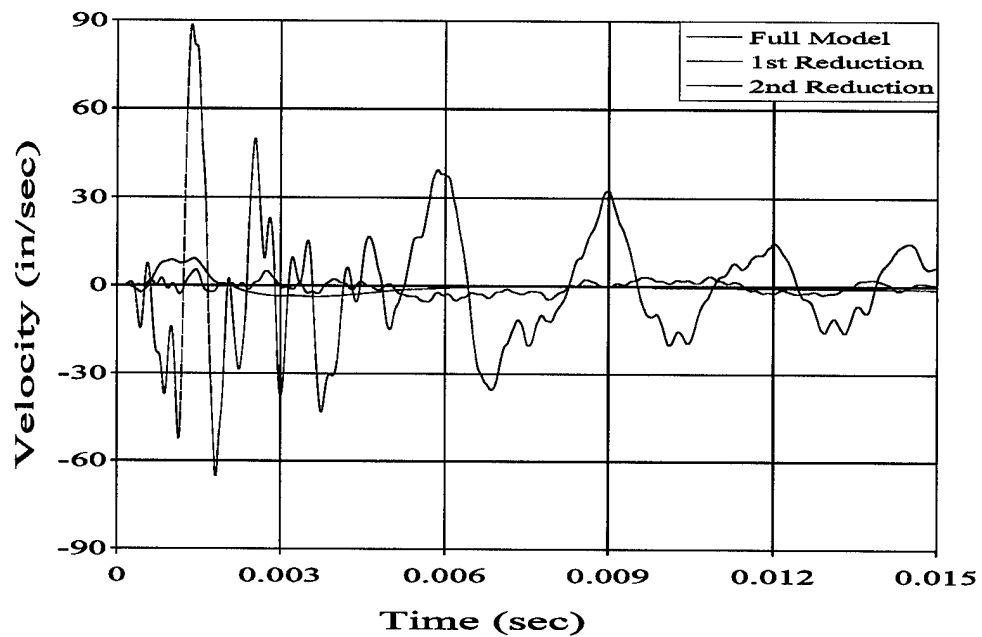## Vertical

Node 86 Resultant Velocity

Figure 21. Large Keel Model, Node 86 Velocity Profiles

39

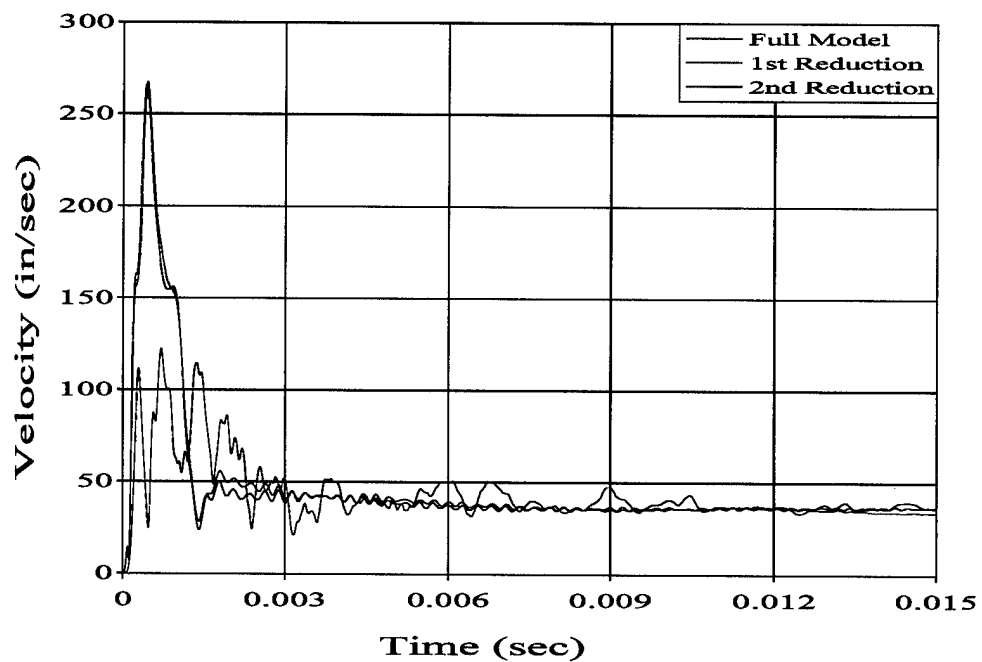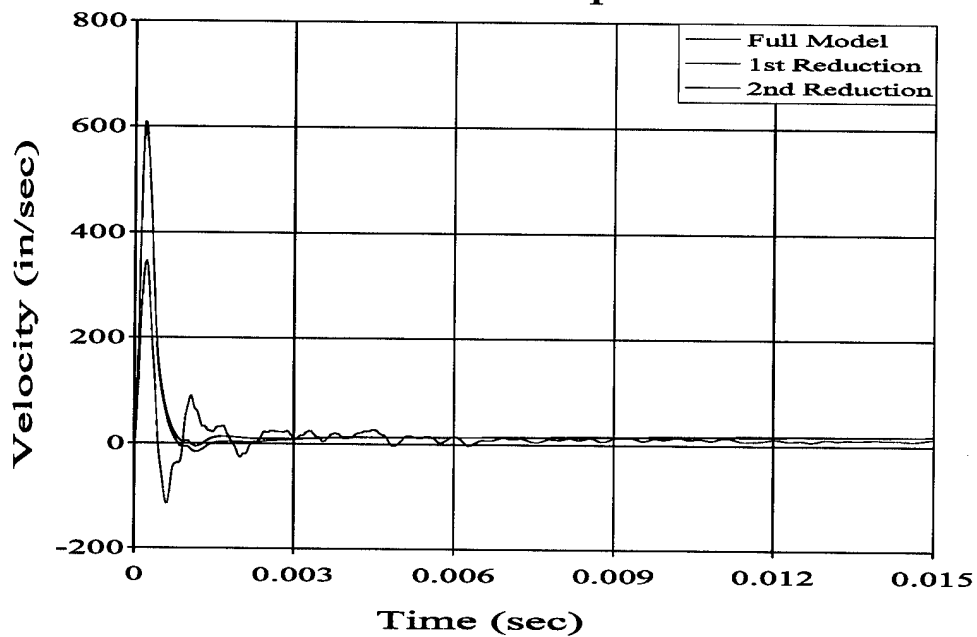# Node 140 Velocity

Fore and Aft

Node 140 Resultant Velocity

Figure 22. Large Keel Model, Node 140 Velocity Profiles

40

Node 157 Velocity

Athwartships
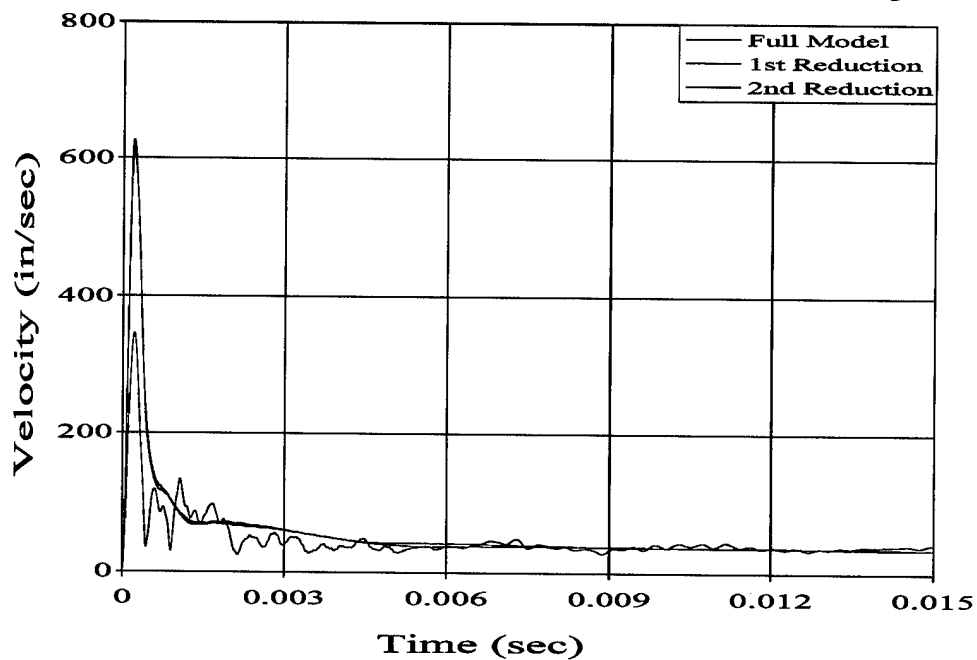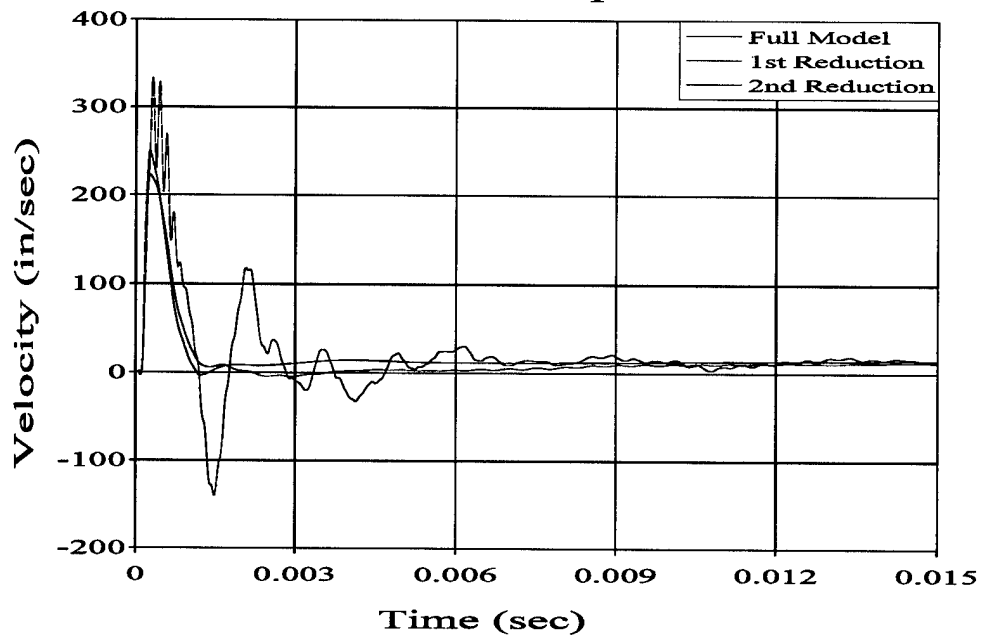

Node 157 Resultant Velocity

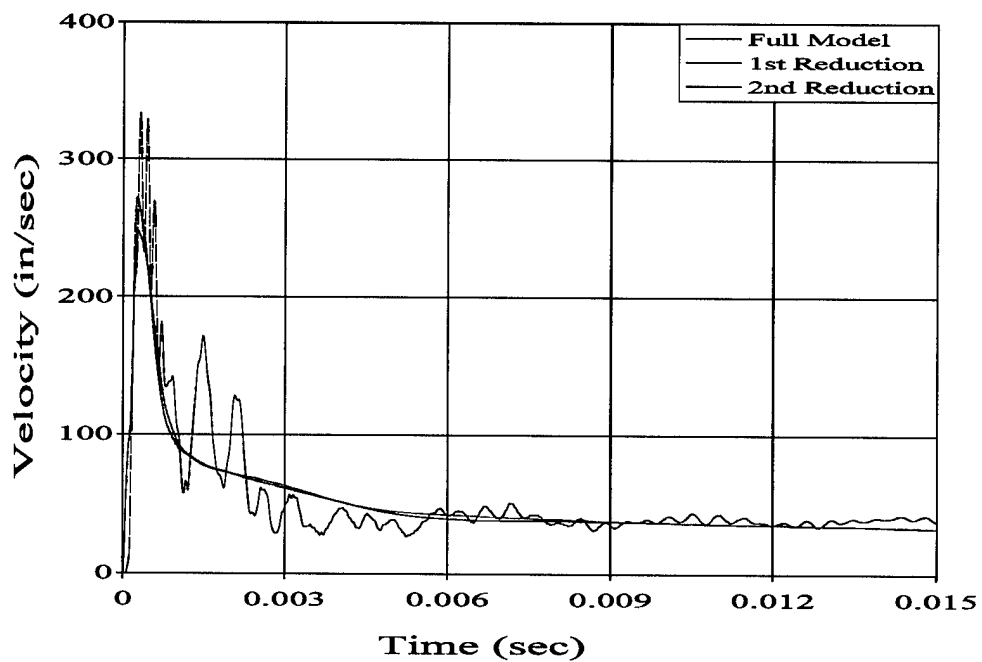**Figure 23. Large Keel Model, Node 157 Velocity Profiles**
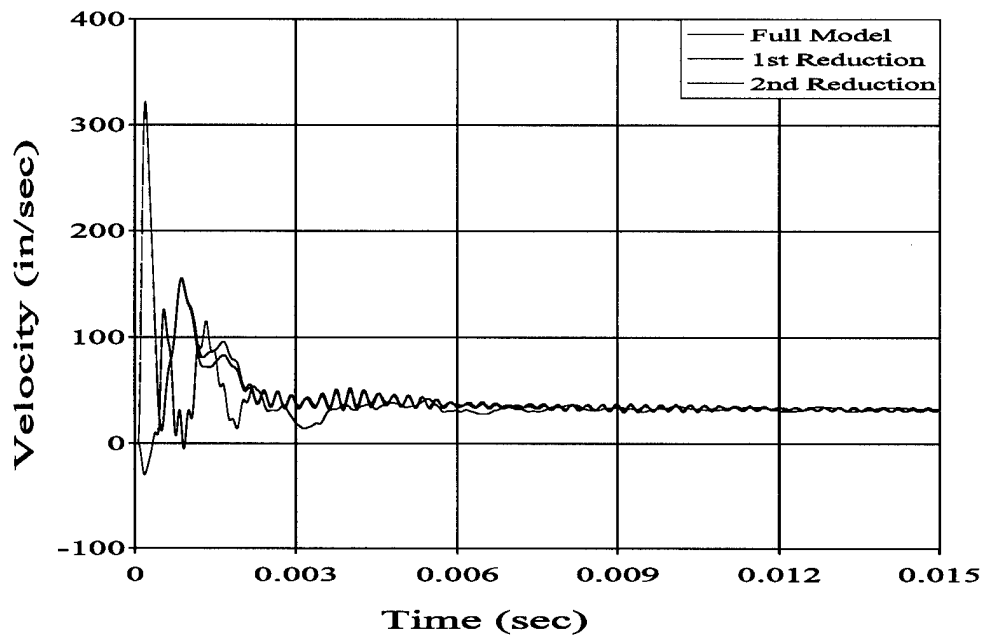
41

Figure 24. Large Keel Model, Node 166 Velocity Profiles

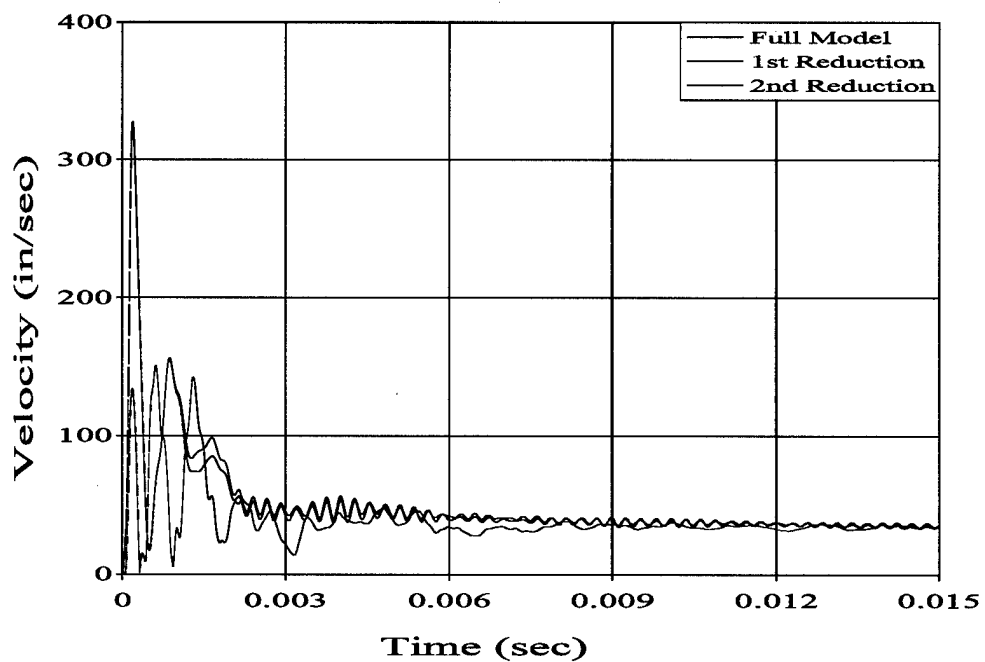# Node 199 Velocity
Vertical

Node 199 Resultant Velocity

**Figure 25. Large Keel Model, Node 199 Velocity Profiles**

	Full Model	1st Reduction	2nd Reduction
Node 55 Athwartships (in/sec)	255.42	68.46	86.94
Node 66 Athwartships (in/sec)	393.09	453.07	444.58
Node 86 Vertical (in/sec)	88.14	209.88	213.10
Node 140 Fore and Aft (in/sec)	88.55	5.34	9.20
Node 157 Athwartships (in/sec)	344.99	608.40	593.49
Node 166 Athwartships (in/sec)	333.47	222.35	249.86
Node 199 Vertical (in/sec)	126.01	321.22	321.94

Table 3. Peak Directional Velocity Values for the Large Keel Model Set

	Full Model	1st Reduction	2nd Reduction
Node 55 (in/sec)	264.79	194.47	206.11
Node 66 (in/sec)	393.38	480.59	472.39
Node 86 (in/sec)	110.80	210.17	213.32
Node 140 (in/sec)	122.46	267.56	266.26
Node 157 (in/sec)	346.19	626.67	612.35
Node 166 (in/sec)	333.72	248.11	272.39
Node 199 (in/sec)	151.19	326.65	327.53

Table 4. Peak Resultant Velocity Values for the Large Keel Model Set

Node 55 Velocity
Athwartships
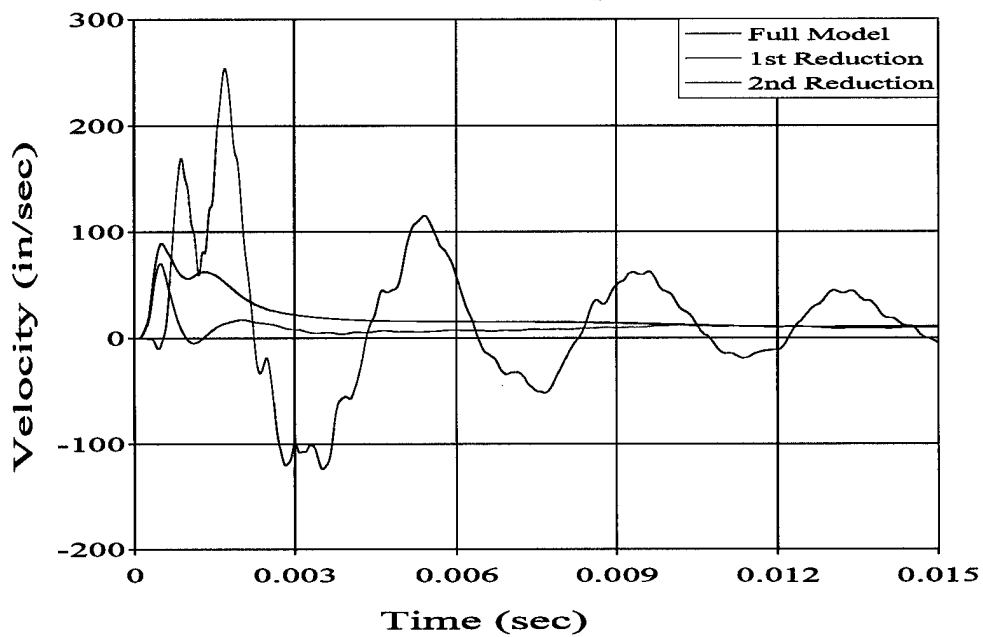
Node 55 Resultant Velocity

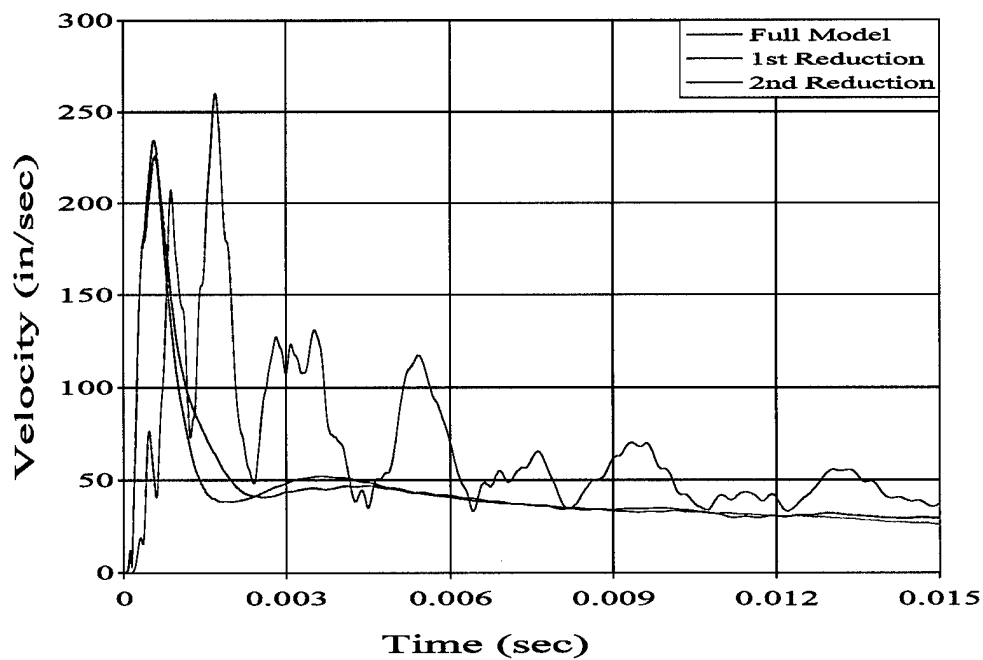**Figure 26. Small Keel Model, Node 55 Velocity Profiles**

45

Figure 27. Small Keel Model, Node 66 Velocity Profiles

Node 86 Velocity

Vertical
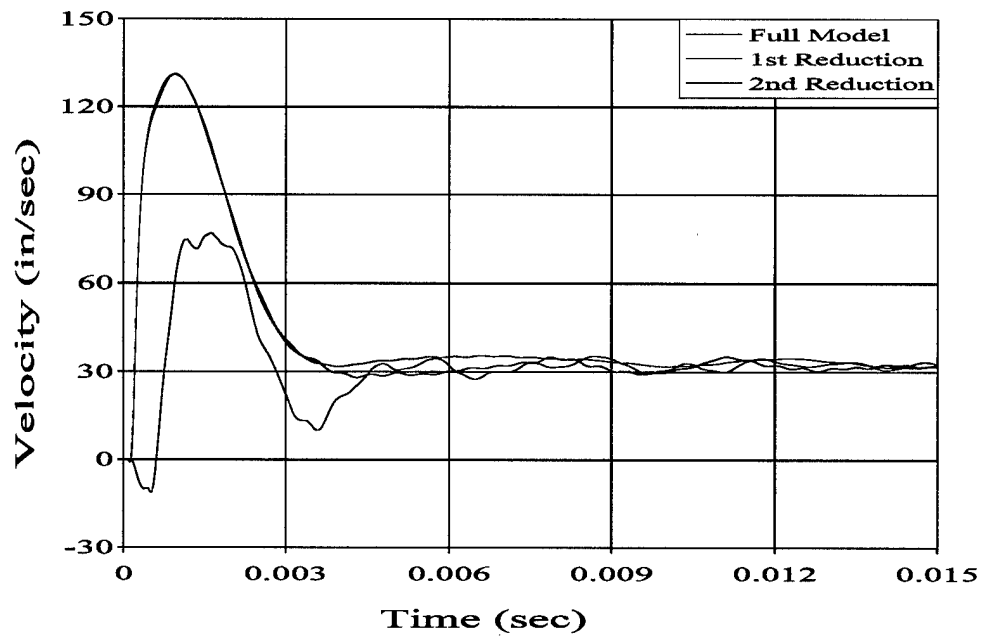
Node 86 Resultant Velocity
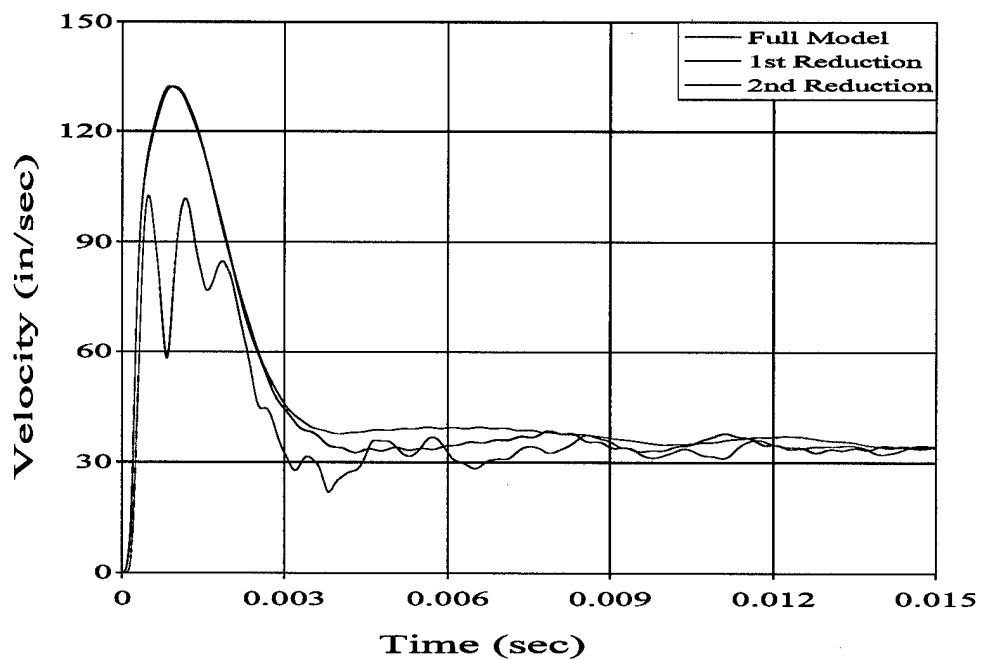
Figure 28. Small Keel Model, Node 86 Velocity Profiles

47

Node 140 Velocity
Fore and Aft
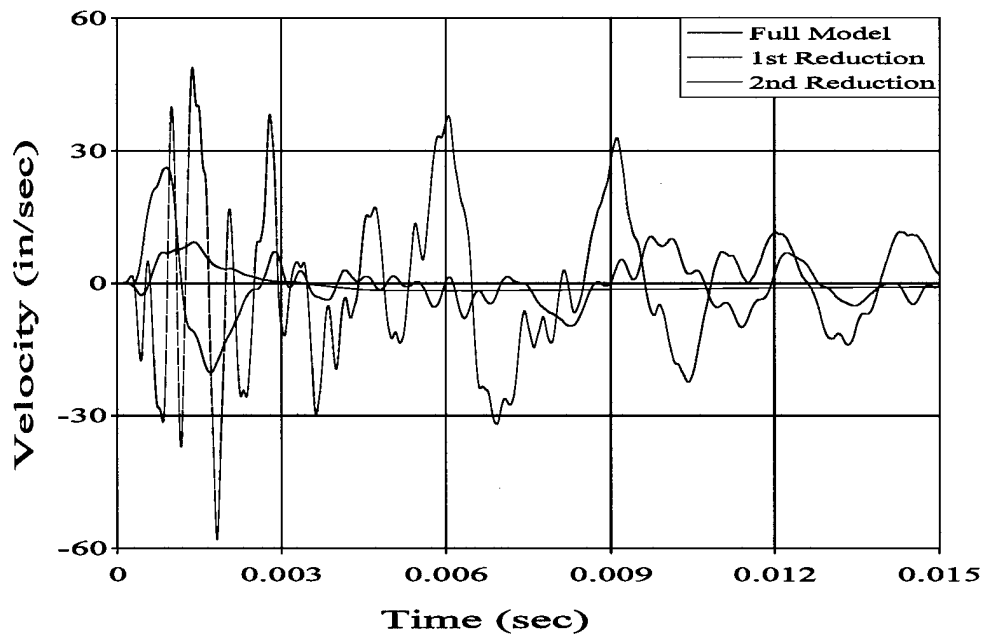
Node 140 Resultant Velocity

Figure 29. Small Keel Model, Node 140 Velocity Profiles

48

Node 157 Velocity
Athwartships

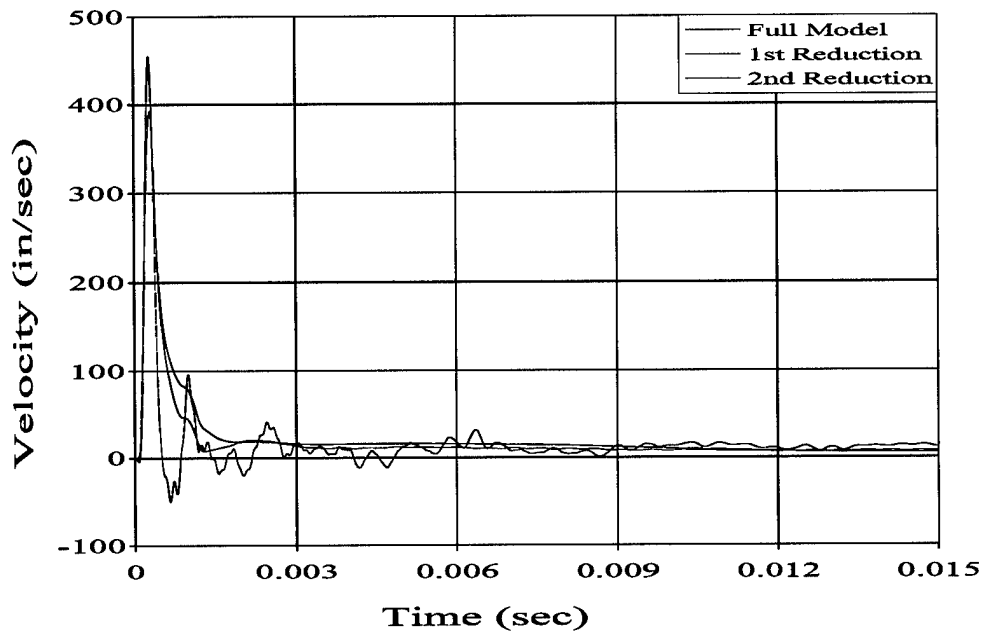# Node 157 Resultant Velocity
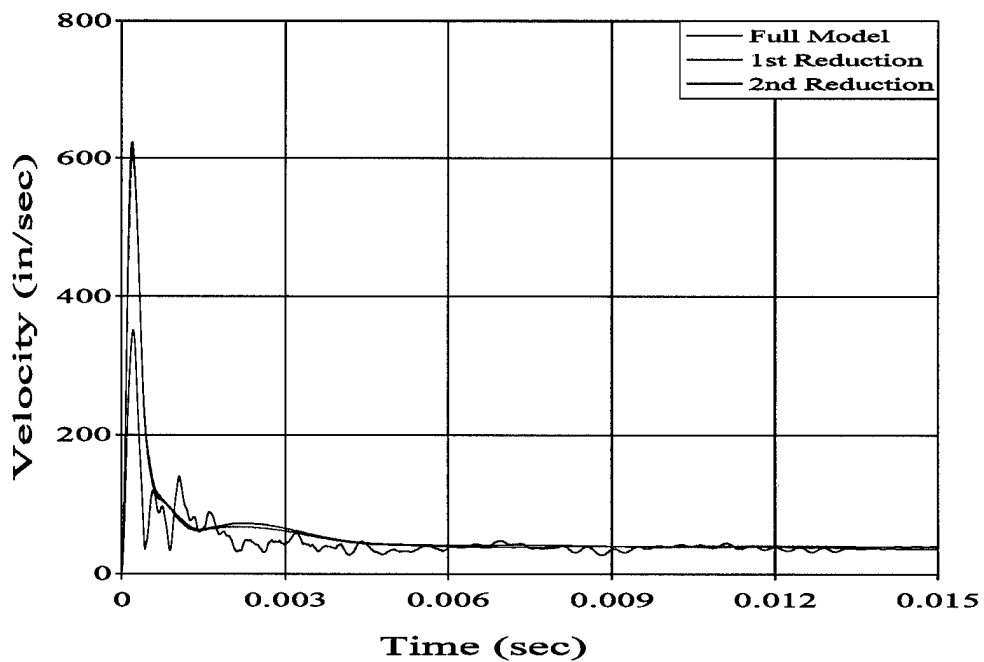
Figure 30. Small Keel Model, Node 157 Velocity Profiles

49

Node 166 Velocity
Athwartships

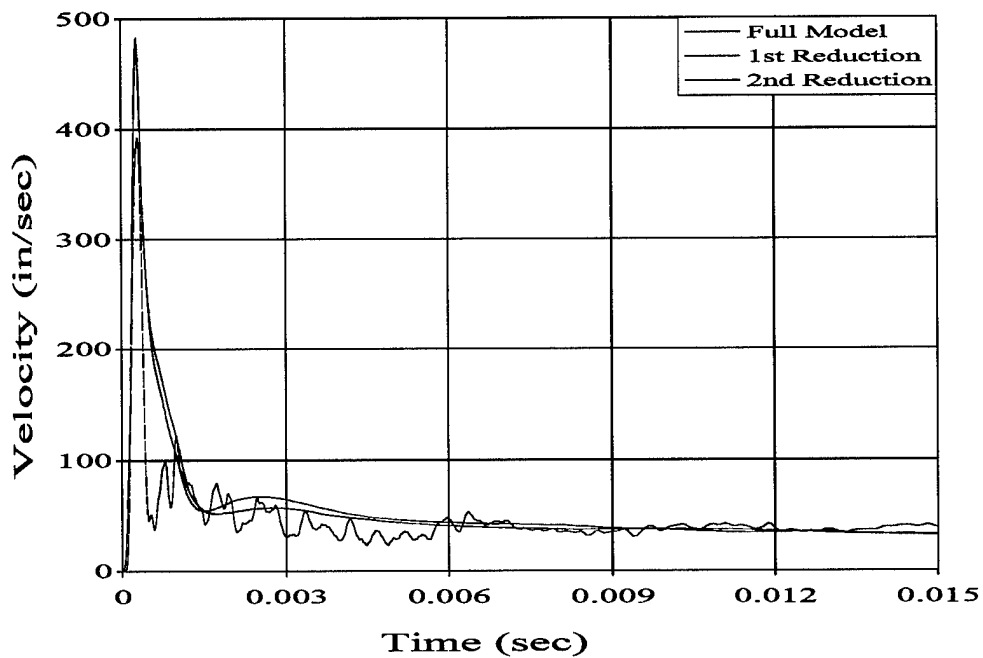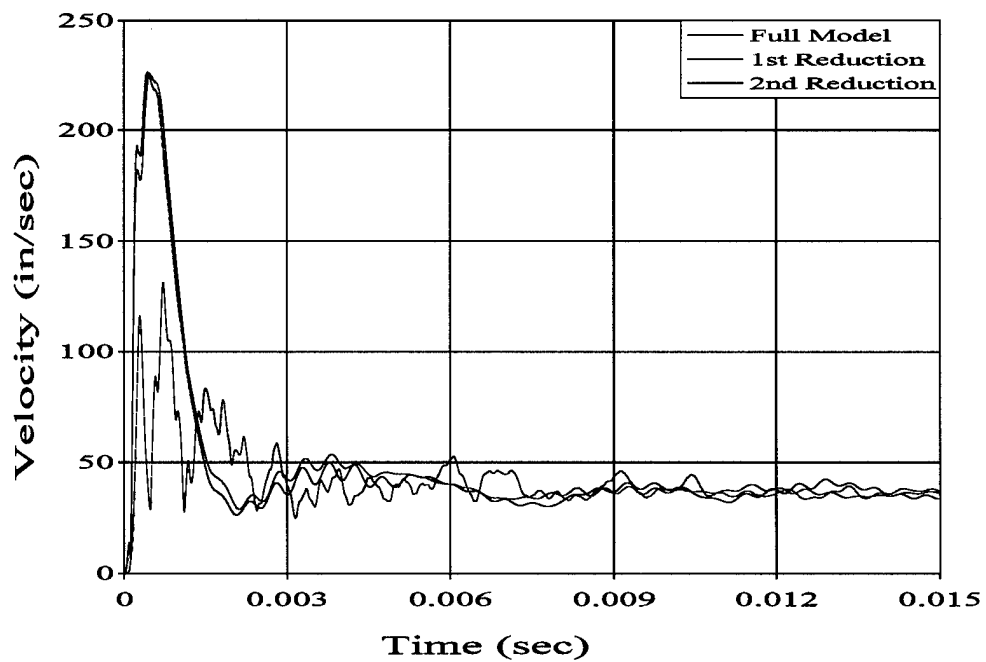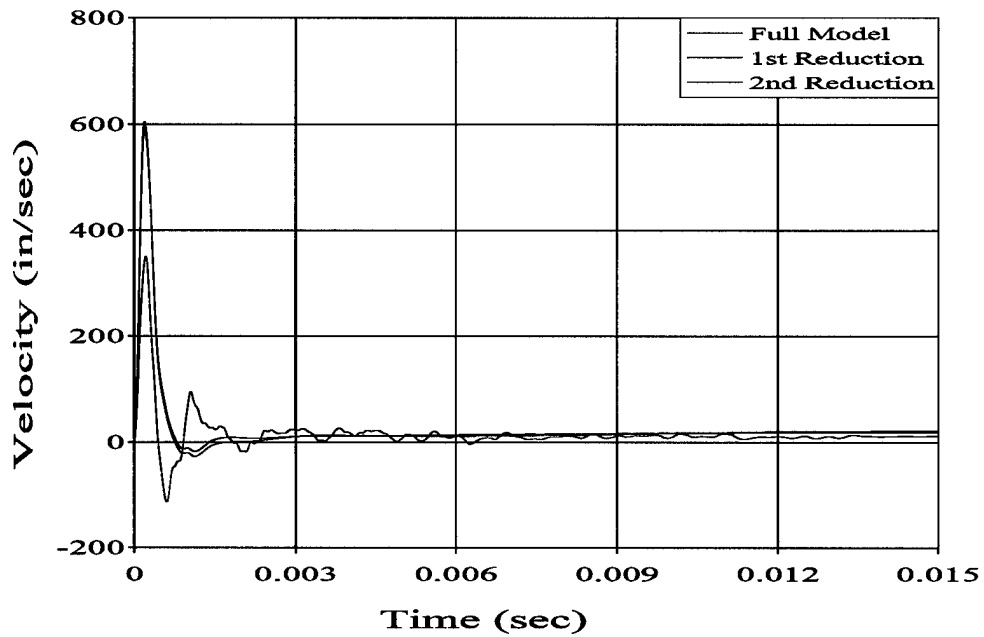

Node 166 Resultant Velocity
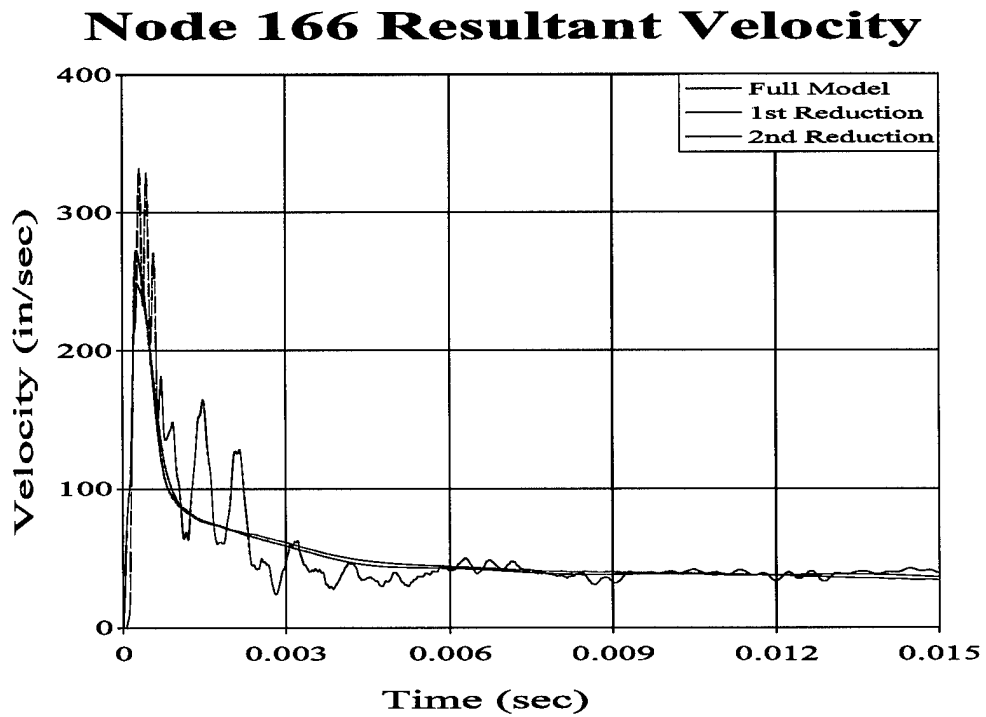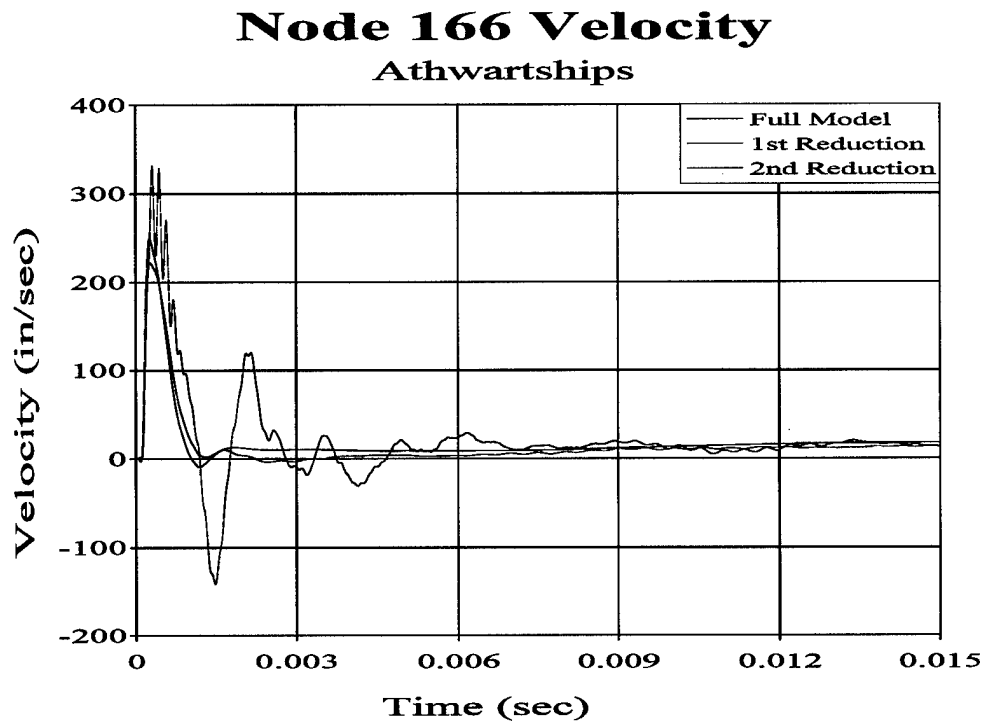
Figure 31. Small Keel Model, Node 166 Velocity Profiles

50

Figure 32. Small Keel Model, Node 199 Velocity Profiles

	Full Model	1st Reduction	2nd Reduction
Node 55 Athwartships (in/sec)	254.16	69.99	89.08
Node 66 Athwartships (in/sec)	392.45	454.58	446.10
Node 86 Vertical (in/sec)	76.88	131.19	131.07
Node 140 Fore and Aft (in/sec)	48.80	26.19	9.39
Node 157 Athwartships (in/sec)	350.13	604.76	589.75
Node 166 Athwartships (in/sec)	331.91	222.37	249.97
Node 199 Vertical (in/sec)	176.16	478.38	479.01

Table 5. Peak Directional Velocity Values for the Small Keel Model Set

	Full Model	1st Reduction	2nd Reduction
Node 55 (in/sec)	260.08	226.15	234.43
Node 66 (in/sec)	392.69	482.86	474.57
Node 86 (in/sec)	102.50	132.31	132.37
Node 140 (in/sec)	131.33	225.98	226.54
Node 157 (in/sec)	351.27	623.05	608.67
Node 166 (in/sec)	332.10	248.55	272.84
Node 199 (in/sec)	212.23	482.94	483.65

Table 6. Peak Resultant Velocity Values for the Small Keel Model Set

V. CONCLUSIONS AND RECOMMENDATIONS

This thesis examined the effects of smearing beam stiffeners into plates on a ship-like box structure that was subjected to an underwater explosion. As the velocity profiles showed, responses for the large keel model were significantly different between the full model and the reduced models in both peak values and oscillation amplitude. Reducing the keel size produced results that were similar to the larger keel case, with the exception of the keel and after bulkhead nodes. These nodes did show sensitivities in velocity response but did not follow any particular trend.

It can be concluded, then, that smearing was not effective in this particular case. The finite element mesh of this box structure was too coarse to produce results that were more comparable between the full model and reduced models. It is considered likely that a more finely meshed box model will display more reliable response results. Computer simulation of surface ship-shock trials is becoming more attractive in view of the rising costs of actual live fire tests and improved smearing techniques will undoubtedly provide more acceptable response results for the underwater shock problem.

Recommended continuing studies in the following areas:

1. Increase the mesh complexity of the finite element box model.

2. Increase the geometric complexity of the box structure to study the smearing effects of more complex models.

3. Model the surrounding fluid in order to include the effects of cavitation on the smeared models.

APPENDIX. USA INPUT DECKS FOR BOX MODEL TEST

The following programs are the FLUMAS, AUGMAT, and TIMINT input decks for the USA code, [Ref. 11].

```
FLUMAS DATA FOR BOX MODEL
flunam geonam strnam daanam        $ FLUNAM GEONAM GRDNAM DAANAM
F F F T                            $ PRTGMT PRTTRN PRTAMF CALCAM
T F F F                            $ EIGMAF TWODIM HAFMOD QUAMOD
F F T F                            $ PCHCDS NASTAM STOMAS STOINV
F F F T                            $ FRWTFL FRWTGE FRWTGR FRESUR
F T F F                            $ RENUMB STOGMT ROTGEO ROTQUA
F F F F                            $ PRTCOE STRMAS SPHERE ROTSYM
F F F F                            $ OCTMOD CAVFLU FRWTFV INTCAV
F F                                $ BOTREF MASREF
0 1001 0 192                       $ NSTRC  NSTRF  NGEN   NGENF
0 0 0                              $ NBRA   NCYL   NCAV
0.9389E-4 59155.2                  $ RHO    CEE
10                                 $ NVEC
12.  0.  0. 1.                     $ DEPTH CXFS CYFS CZFS
14.7 386.088                       $ PATM GRAVAC
0                                  $ NSRADI
0                                  $ NSORDR


AUGMAT DATA FOR BOX MODEL
strnam flunam geonam prenam        $ STRNAM FLUNAM GEONAM PRENAM
F F F F                            $ FRWTGE FRWTST FRWTFL LUMPFM
F T F T                            $ FLUSKY DAAFRM SYMCON DOFTAB
F F F F                            $ PRTGMT PRTTRN PRTSTF PRTAUG
F F F F                            $ MODTRN STRLCL INTWAT CFADYN
4                                  $ NTYPDA
0.5                                $ DAA2M
1001 3003 3 3                      $ NSTR   NSFR   NFRE   NFTR
1                                  $ NSETLC
0 1 192 1                          $ NDICOS JSTART JSTOP  JINC
```

```
TIMINT DATA FOR BOX MODEL
prenam posnam           $ PRENAM POSNAM
resnam                  $ RESNAM WRTNAM
F F                     $ REFSEC FLUMEM
1                       $ NTINT
0.0 1.0E-6              $ STRTIM DELTIM
T F F F                 $ EXPWAV SPLINE VARLIN PACKET
F T F F                 $ HYPERB EXPLOS DOUBDC VELINP
F F                     $ BUBPUL SHKBUB
1                       $ NCHARG
0.                      $ HYDPRE
60.0 -100.44 -174.00    $ XC      YC      ZC
55.2 -12. 0.            $ SX      SY      SZ
201                     $ JPHIST
1. 0.                   $ PNORM   DETIM
4.765E-6                $ DTHIST
1                       $ CHGTYP
20. 16.75 15.50         $ WEIGHT SLANT CHGDEP
2000 2000               $ NSAVER NRESET
0 0 0 0                 $ LOCBEG LOCRES LOCWRT NSTART
F F F                   $ FORWRT STBDA2 ASCWRT
F                       $ DISPLA
```

LIST OF REFERENCES

1. OPNAV Instruction 9072.2, "Shock Hardening of Surface Ships", January 1987.

2. USS John Paul Jones (DDG-53) Shock Trial Final Report, AEGIS Program Manager (PMS-400), November 1994.

3. Cole, R.H., *Underwater Explosions*, pp. 3-13, Princeton University Press, 1948.

4. Shin, Y.S., "Naval Ship-Shock and Design Analysis", Course Notes for Underwater Shock Analysis, Naval Postgraduate School, Monterey, CA, 1996.

5. Geers, T.L., "Residual Potential and Approximate Methods for Three-Dimensional Fluid-Structure Interaction Problems", The Journal of the Acoustical Society of America, Vol. 49, pp. 1505-1510, 1971.

6. DeRuntz, J.A. Jr., "The Underwater Shock Analysis Code and Its Applications", Paper presented at the 60th Shock and Vibration Symposium, Vol. I, pp. 89-107, November 1989.

7. XYZ Scientific Applications, Inc., *TrueGrid®: A Quality Mesh in a Fraction of the Time*, Livermore, CA, 1997.

8. MacNeal-Schwendler Corporation, *MSC/PATRAN Installation and Operations Guide*, Version 7.0, Publication No. 903002, Los Angeles, CA, July 1997.

9. Livermore Software Technology Corporation, *LS-DYNA Keyword User's Manual*, Version 940, Livermore, CA, 1997.

10. S. Timoshenko, S. Woinowsky-Kreiger, *Theory of Plates and Shells*, McGraw-Hill, NY, 1959.

11. Shin, Y.S., DeRuntz, J.A., "USA/LS-DYNA3D Software Training Course", Vol. V, July 1996.

INITIAL DISTRIBUTION LIST

No. of Copies

1. Defense Technical Information Center   2
   8725 John J. Kingman Rd., Ste 0944
   Ft. Belvoir, VA 22060-6218

2. Dudley Knox Library   2
   Naval Postgraduate School
   411 Dyer Rd.
   Monterey, CA 93943-5101

3. Professor Young S. Shin, Code ME/Sg   2
   Department of Mechanical Engineering
   Naval Postgraduate School
   Monterey, CA 93943

4. Professor Y.W. Kwon, Code ME/Kw   1
   Department of Mechanical Engineering
   Naval Postgraduate School
   Monterey, CA 93943

5. Naval/Mechanical Engineering Curricular Office (Code 34)   1
   Department of Mechanical Engineering
   Naval Postgraduate School
   Monterey, CA 93943

6. LT Keith A. Beiter   5
   404 Warley St.
   Newport, RI 02871

7. Michael Winnette   1
   Naval Surface Warfare Center, Carderock Division
   Underwater Explosions Research Department
   1445 crossways Blvd.
   Chesapeake, VA 23320

8. Fred Costanzo   1
   Naval Surface Warfare Center, Carderock Division
   Underwater Explosions Research Department
   1445 Crossways Blvd.
   Chesapeake, VA 23320